Geothermics 140 (2026) 103682

Contents lists available at ScienceDirect

Geothermics

journal homepage: www.elsevier.com/locate/geothermics

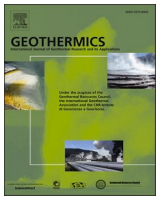

Integrated geophysical insights into the structural controls on geothermal systems in the Tatun Volcano group, northern Taiwan

T. Lan-Chi Nguyen [a], Wen-Jeng Huang [a,b,*], Chien-Chih Chen [a,b], Chi-Shu Yen [b], Yi-Heng Li [c], Horng-Yuan Yen [b]

[a] Institute of Applied Geology, National Central University, Taoyuan City, Taiwan
[b] Department of Earth Sciences, National Central University, Taoyuan City, Taiwan
[c] Industrial Technology Research Institute, Tainan City, Taiwan

ARTICLE INFO

Keywords:
Tatun Volcano group (TVG)
Geothermal exploration
Magnetotelluric (MT)
Fault-controlled geothermal system

ABSTRACT

Geothermal systems suitable for power generation require sufficient temperatures, favorable structural conditions, and reservoir permeability at depths shallower than ~3–5 km. This study investigates geothermal resources and prospective development sites in the Tatun Volcano Group (TVG), northern Taiwan, using a new magnetotelluric/audio-magnetotelluric (MT/AMT) dataset integrated with gravity, magnetic, microseismic, borehole, and geological information. A 3D resistivity model was constructed from MT inversion, and seven geological cross-sections were developed using the kink method and refined with multiple geophysical constraints to relate resistivity structures to subsurface geology. Two geothermal systems are identified—the Mt. Qixing–Matsao–Mt. Shamao and Mt. Huangzui–Dayoukeng–Mt. Dajianhou systems—each characterized by a low-resistivity clay cap (<10 Ωm) overlying a moderately resistive reservoir (10–60 Ωm). A deep high-resistivity batholith and steep intrusive bodies spatially align with the Jin-shan and Shan-chiao faults. Both geothermal systems occur within hanging-wall domains, which also host dense microseismic clusters, whereas adjacent footwalls consist of either high-resistivity volcanic units or thick conductive altered zones, both indicative of low-permeability conditions that inhibit fluid flow. These relationships demonstrate that fault architecture governs the localization of fractured reservoirs and hydrothermal upflow pathways. We interpret the batholith as the principal magmatic heat source and the fault-controlled structural framework as the primary regulator of reservoir distribution. Together, these findings highlight the hanging-wall regions of the Jin-shan and Shan-chiao faults as priority targets for future geothermal exploration and development in the TVG.

1. Introduction

Geothermal energy represents a sustainable and low-carbon energy resource, particularly in volcanic regions where high heat flow and active magmatic systems provide favorable thermal conditions. Geothermal systems are controlled by three key factors: (1) heat sources; (2) permeability along faults, fractures, and geological formations; and (3) fluid flow patterns, including large-scale convection, recharge, and fluid chemistry (Jolie et al., 2021; Moeck, 2014). These geological controls operate across multiple scales—from local fracture networks within the reservoir to regional tectonic activities—well performance often varies dramatically within and among geothermal fields. Therefore, effective geothermal exploration depends on understanding how geological structures interact to control permeability, heat transfer, and fluid circulation (Moeck, 2014). Understanding subsurface geological structures is essential for the effective exploration and development of geothermal resources, a cornerstone of sustainable energy strategies. (e.g. Guglielmetti et al., 2013). Surface geology alone is often insufficient for accurately inferring structures at depths greater than several hundred meters, in geologically complex volcanic–tectonic settings such as the Tatun Volcano Group (TVG) in northern Taiwan. Therefore, various geophysical methods have been employed to investigate the subsurface architecture of the TVG. These include electrical resistivity surveys (e.g., Cheng, 1970), magnetic and gravity studies (Yang et al., 1994), and seismic tomography (e.g., Huang et al., 2021; Lin et al., 2005; and Lin et al., 2024; Pu et al., 2020, 2025).

Electrical resistivity is widely used in volcanic geothermal exploration because it is sensitive to temperature, fluid content, and

* Corresponding author.
E-mail address: huang22@ncu.edu.tw (W.-J. Huang).

https://doi.org/10.1016/j.geothermics.2026.103682
Received 10 December 2025; Received in revised form 27 February 2026; Accepted 30 March 2026
Available online 30 April 2026

hydrothermal alteration. Hydrothermal processes typically produce a characteristic three-layer structure consisting of (1) the unaltered young volcanic zone (>100 Ωm), (2) the conductive clay cap (<10 Ωm), and (3) the underlying moderately resistive reservoir (10–60 Ωm) (Johnston et al., 1992; Cumming, 2009; Cumming and Mackie, 2010; Stimac et al., 2015). This resistivity stratification provides an effective framework for identifying clay caps and geothermal reservoirs.

Early investigations of geothermal activity at the TVG identified hydrothermal alteration and shallow conductive anomalies using magnetic, vertical electrical soundings (VES), AMT, and VLF-MT surveys (Cheng, 1970; Komori et al., 2014, 2017). Seismic tomography and microseismic studies later revealed deep low-velocity anomalies and possible magmatic conduits beneath Mt. Qixing, Dayoukeng, and Mt. Huangzui, indicating an active magmatic heat source (Huang et al., 2021; Pu et al., 2020, 2025). Despite previous efforts, earlier geophysical surveys lacked the spatial resolution necessary to constrain the geometry, thickness, and continuity of clay caps and geothermal reservoirs, and they were not integrated into a unified geothermal framework. Consequently, the relationships among alteration zones, reservoir structure, and major fault systems have remained insufficiently resolved.

To address these limitations, this study employs a new high-resolution magnetotelluric (MT) dataset comprising 47 stations acquired between 2020 and 2023, integrated with gravity, magnetic, microseismic, borehole, and geological data. A fully 3D resistivity model is constructed and combined with structurally geological cross-sections to investigate the subsurface architecture of the TVG.

Building upon recent geological and geophysical findings, this study aims to improve the understanding of the TVG geothermal system through the following objectives: (1) delineate the potential geothermal system (clay-cap and reservoir structure) using 3D MT resistivity model; (2) construct detailed geological cross-sections along NW–SE and NE–SW transects to clarify fold geometries, fault configurations, and stratigraphic relationships, thereby illuminating structural controls on fluid pathways and (3) evaluate how major fault systems control reservoir localization and hydrothermal circulation. By integrating multidisciplinary datasets within a structural framework, this study refines the conceptual model and constructs a semi-3D geological model of the TVG geothermal system and provides guidance for future exploration and drilling strategies in northern Taiwan.

2. Geological background

The Tatun geothermal field is hosted in the TVG in the northwest corner of Taiwan (Fig. 1a). This area was identified as a promising geothermal exploration target due to the presence of numerous hot springs and fumaroles indicating an underlying active magmatic heat source. Its proximity to Taipei, a metropolis of 6.9 million people, further underscores its strategic importance for geothermal energy development, offering a sustainable and renewable energy alternative.

Taiwan is situated at the junction of the Eurasian Plate and the Philippine Sea Plate (Fig. 1a), and has formed as a result of their ongoing collision. The TVG is part of the North Taiwan Volcanic Zone (NTVZ), located near the southern end of the Okinawa Trough (Fig. 1a). Offshore northeastern Taiwan, the ongoing subduction of the Philippine Sea Plate has generated the Ryukyu volcanic arc and submarine volcanoes within the Okinawa Trough, while the NTVZ—from offshore to inland—is interpreted to have developed from mountain belt collapse driven by extension (Lin et al., 2024; Teng, 1996). This subduction-related magmatism has contributed significantly to the emergence of the TVG as an important Quaternary volcanic system (Teng, 1996). Moreover, the TVG is associated with the post-collisional extension of the Taiwan orogen, which has further influenced its volcanic activity and enhanced its geothermal potential (Chang et al., 2024; Huang et al., 2021).

The TVG is delineated by the Kan-chiao fault to the southeast and is geographically transected by the Tamsui River in the southwest (Fig. 1b). The majority of volcanic edifices are situated northeast of the river, with only two out of the 51 identified edifices situated to the

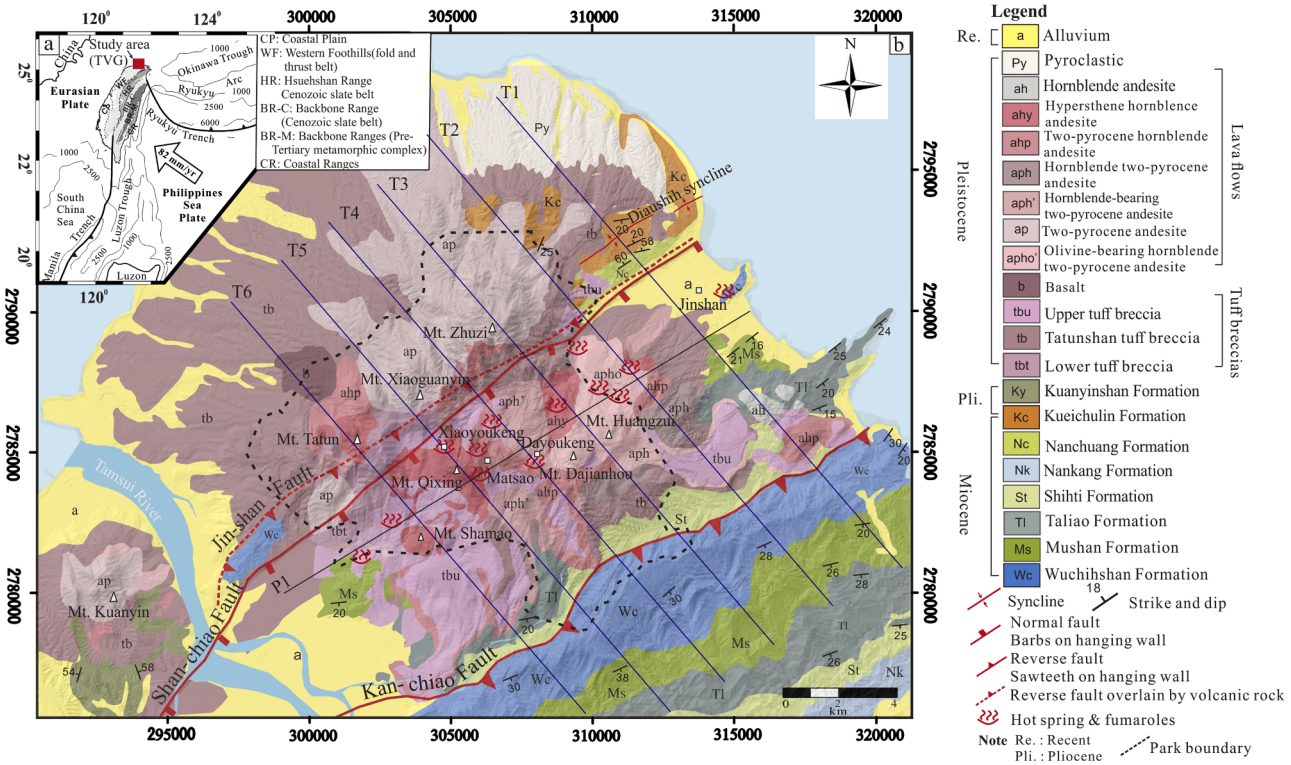

Fig. 1. (a) Regional tectonic setting of Taiwan and its surrounding subduction system, including the Ryukyu volcanic arc and Okinawa Trough (compiled from Shyu et al., 2005; Teng, 1996; Yu et al., 1997). (b) Geological map of the Tatun Volcano Group (TVG), showing major volcanic edifices and fault structures (adapted from Taiwan Central Geological Survey, 2005).

southwest, as reported by Chen et al. (2007). These volcanic structures are predominantly composed of andesitic rocks. Traditionally, the TVG was regarded as a dormant or extinct volcanic system, given the absence of historically recorded eruptions (Kim et al., 2005; Konstantinou, 2014). However, recent investigations have revised this interpretation. Volcanic ash deposits retrieved from the northern Taipei Basin, along with volcaniclastic layers within the TVG, suggest that eruptions occurred as recently as ~6000 years ago, with activity extending back to around 23,000 years before present (Belousov et al., 2010; Chen et al., 2002, 2010). Moreover, zircon U–Pb geochronology conducted by Chu et al. (2018) indicates that magmatic activity in the TVG initiated around 3 million years ago (Ma), became more vigorous after approximately 0.8 Ma, and reached a pronounced flare-up phase around 0.35 Ma. Most volcanic activity occurred within the past 0.8 Ma, with eruptive events likely ceasing around 0.2 Ma.

The TVG is situated within Miocene to Pleistocene sedimentary strata of the fold-and-thrust belt in the northern Taiwan orogenic system. This belt developed in response to the convergence between the Philippine Sea Plate and the Eurasian Plate since approximately 6 Ma (Lin et al., 2003; Fig. 1). These sedimentary units are primarily exposed along the periphery of the TVG and to the southeast of the Kan-chiao thrust fault. This fault trends northeast–southwest, extending from the northern coastline to the Tamsui River. The Kan-chiao thrust fault is generally interpreted to dip at an angle of ~30° or less (e.g., Huang et al., 1991). Approximately 9 km to the northwest, the Jin-shan thrust fault runs subparallel to the Kan-chiao fault. First identified by Ooe and Ogasawara (1934), this fault was recognized by a distinct lithological contrast across the unseen fault zone at the northern margin of the Jin-shan Plain. Adjacent and subparallel to the Jin-shan fault lies the Shan-chiao Normal Fault, which transects regions dominated by volcanic rocks and pyroclastic deposits (Fig. 1b). Both the Kan-chiao thrust fault and Jin-shan thrust fault are interpreted as products of crustal shortening during the contractional tectonic phase that spanned from 6 to 0.8 Ma (Teng et al., 2001). In contrast, the Shan-chiao normal fault is attributed to subsequent extensional tectonism, active since ~0.8 Ma (Teng et al., 2001). The area between the two major thrust faults is characterized by numerous subsidiary faults and fracture systems, which have resulted from both tectonic deformation and volcanic processes. Under the current extensional regime, many northeast–southwest-oriented faults have evolved into open fissures. These fissures serve as vital conduits for the migration of hydrothermal fluids and are strongly associated with active hot springs (Song, 2000). Notably, fissures on the southeastern and northwestern flanks of Mt. Qixing, as well as near Mt. Huangzui (Fig. 1b), are closely linked to geothermal phenomena, including hot springs, fumaroles, and zones of hydrothermal alteration (Song, 2000).

These complex geological structures, including thrust and normal faults, volcanic edifices, and hydrothermal features, not only shape the surface landscape of the TVG but also influence subsurface fluid flow and geothermal potential. However, given the limitations of surface geology in revealing deep structural frameworks, geophysical investigations are essential to better understand the architecture and dynamics of the underlying geothermal system.

3. Methods and data

3.1. MT method and data

The magnetotelluric (MT) method characterizes subsurface resistivity by measuring natural variations in the Earth's electromagnetic (EM) fields. These fields originate from natural sources (e.g., solar–ionospheric interactions), and are generated outside the Earth's subsurface. Variations in Earth's resistivity slightly modify the EM fields measured at the surface. MT data processing involves converting time series of electric and magnetic fields into frequency-domain transfer functions, such as the impedance tensor, from which subsurface resistivity can be inferred.

MT data in the TVG area were acquired using the Phoenix MTU-5C system (Phoenix Geophysics, Toronto, Canada) through a two-stage survey. The first stage comprised 42 stations selected from the 49 stations originally collected by the Industrial Technology Research Institute (ITRI, 2021) and later processed and interpreted by Chen et al. (2023). The original MT data were independently re-evaluated and reprocessed in this study to ensure consistent data quality control and noise suppression. A few stations that exhibited high site-specific noise or unstable impedance tensors were excluded from further analysis. In addition, five new MT stations were deployed by the National Central University (NCU) to cover data gaps in the TVG, particularly near Mt. Qixing, an area previously recognized as a likely up-flow zone from integrated geophysical evidence (Chen et al., 2023; Pu et al., 2020; and Pu et al., 2025).

The current 47 soundings span periods from 1×10^{-4} s to approximately 2.5×10^{3} s, corresponding to a frequency range of 0.4 mHz–10 kHz, enabling improved imaging from the shallow geothermal system to deeper structures. Stations were distributed across the major fault zones and geothermal features in the TVG. The inter-station spacing generally ranged from about 1–2 km, but locally exceeded 4 km in a few areas where site conditions limited station deployment (Fig. 2). Remote reference techniques were applied to improve signal quality: in the first stage, a reference site was installed in Tainan (~232 km south of the TVG); in the second stage, another was added in Yilan (~50 km east of the TVG). All 47 stations were ultimately inverted together in a unified 3D inversion.

At each station, two orthogonal horizontal electric field components, Ex and Ey, were measured in the north-south and east-west directions, respectively. Magnetic field components Hx, Hy, and Hz corresponding to the north-south, east-west, and vertical orientations were also recorded. Due to rugged terrain and logistical constraints, electrodes were spaced approximately 20–30 m apart. Magnetic sensors were positioned approximately 10–15 m from the recording unit to minimize mutual interference. Data acquisition durations at individual stations ranged from 40 h to 8 days. Extended recording times were essential to capture low-frequency signals and improve data quality, particularly during nighttime, when anthropogenic EM noise is lower and natural signal strength increases.

The purpose of pre-processing is to convert time series data of EM fields into MT impedance and tipper functions in the frequency domain. The Phoenix Geophysics' EMPower software was used to process the raw data in time domain and turned it into the frequency domain expressions that included each station's apparent resistivities and impedance phases as a function of frequency. Then, the 3D-Grid and ModEM (Egbert and Kelbert, 2012; Kelbert et al., 2014) programs were used to post-process and invert the spectral data.

Apparent resistivity represents the averaged resistivity of the Earth from the surface to the maximum depth reached by the EM signal. When apparent resistivity is plotted against decreasing frequency, this corresponds to increasing penetrated depth within the Earth of the EM signal. In MT surveys, each sounding yields a complex impedance tensor relating the horizontal electric and magnetic field components. The off-diagonal components, Zxy and Zyx, are commonly examined in sounding curves and provide diagnostic information on subsurface resistivity variations. Differences between these components, as well as the behavior of the diagonal terms, offer insight into whether the subsurface resistivity structure is predominantly one-dimensional (1D), two-dimensional (2D), or three-dimensional (3D). Representative apparent resistivity curves derived from selected MT stations (47 in total) in the TVG geothermal field are shown in Fig. 3. As the period grows till ~1 s, the apparent resistivities of both modes gradually decrease from high values for short periods (< 0.01 s). After that, the apparent resistivity increases up to a period of 10 s. MT-sounding curves have the potential to reveal detailed resistivity structures that could be inferred from further modeling and inversion.

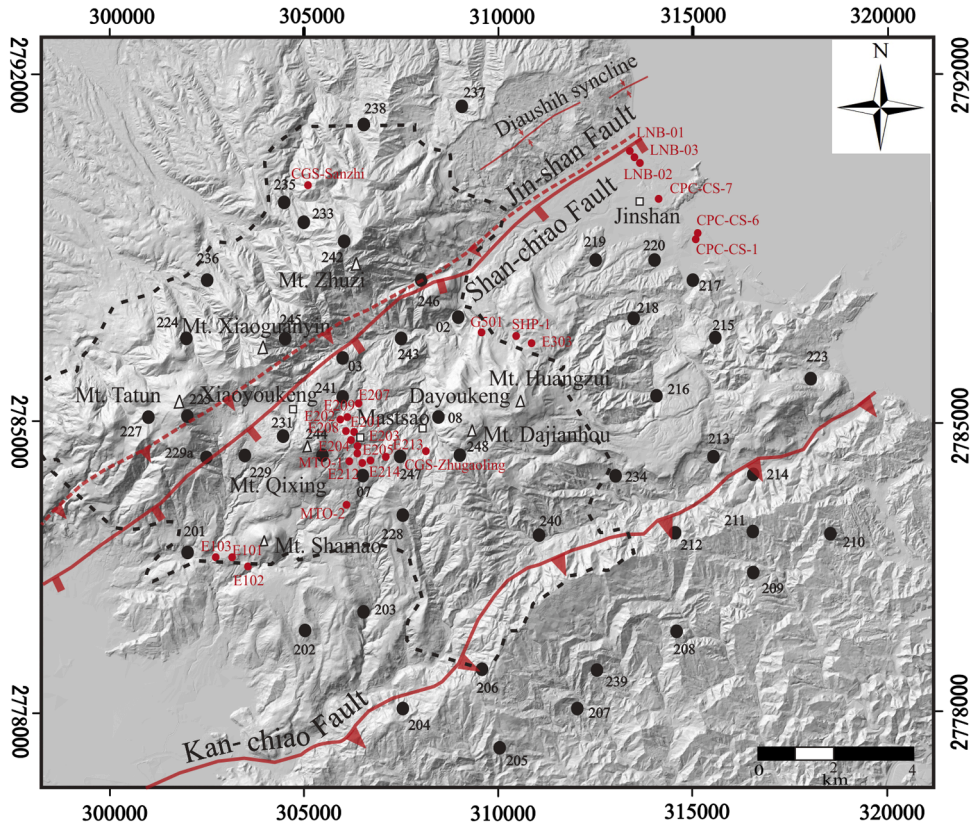

Fig. 2. Distribution of MT stations in the TVG area. The base map shows topography. MT stations are indicated by black dots, and boreholes by red dots. The black dashed line marks the boundary of Yangmingshan National Park. The hillshade basemap was produced using the open-access 20 m Digital 125 Terrain Model (DTM) provided by Taiwan's National Land Surveying and Mapping Center 126 (Dataset 138563, https://data.gov.tw/dataset/138563).

The ModEM software (Egbert and Kelbert, 2012; Kelbert et al., 2014) was applied to carry out the fully 3D inversion of MT data, and the results were subsequently displayed using the 3D-Grid software (Egbert and Kelbert, 2012; Kelbert et al., 2014). The initial model included a 62 × 64 × 71 cell grid along the x, y, and z axes, respectively, and assumed a uniform resistivity of 100 Ωm for half-space and 0.3 Ωm for seawater. Vertically, the model had 72 layers, with layer thickness increasing by a factor of 1.3. A custom MATLAB tool was developed to facilitate the export of resistivity profiles in any desired direction, supplementing the standard N–S and E–W outputs of 3D-Grid. The 3D inversion was performed using the ModEM algorithm, which minimizes a regularized penalty functional that balances data misfit and model smoothness (Egbert and Kelbert, 2012; Kelbert et al., 2014):

$$\Phi(m,d) - (d - F(m))^T C_d^{-1}(d - F(m)) + \nu(m - m_0)^T C_m^{-1}(m - m_0) \quad (1)$$

The discrepancy between the measured data d and the model response, F(m), is the data misfit, represented by the first term in the right-hand side in Eq. (1). The estimated model m is compared to the original model m_0 in the second term, which represents the model update. The regularization parameter is represented by ν, while the data and model covariances are denoted by the terms C_d and C_m, respectively. A line search approach is used to update the original model m_0.

The reliability of the MT inversion was evaluated using the complete set of sounding curves and misfit statistics for all stations. Across the dataset, the modeled responses closely reproduce the measured apparent resistivities and phases for both Zxy and Zyx components over the full frequency range. For most sites, the inversion captures the principal characteristics of the MT data, including the shapes of the apparent resistivity curves, frequency-dependent inflection points, and the separation between the two impedance modes.

The sounding curves shown in Fig. 3 demonstrate stable behavior in both the amplitude and phase components of the impedance tensor across representative stations. Apparent resistivity values for Zxy and Zyx decrease smoothly by approximately 1.0–1.5 log units (e.g., from ~80–100 Ωm at 10^{-4}–10^{-3} s to ~3–10 Ωm at 10^{0}–10^{1} s), with measured and predicted curves differing by less than ~0.05–0.15 log units for most frequencies. Phase responses likewise vary in a physically realistic and monotonic manner, typically remaining within –90° to +60° and showing no wrapping or discontinuities. The inversion also reproduces the observed separation between Zxy and Zyx modes, with characteristic phase differences of 20°–40° at mid periods and convergence at longer periods.

These quantitative agreements—smooth curve slopes, consistent mode separation, and low residual differences—indicate that the inversion has converged to a physically meaningful resistivity structure.

Total nRMS values provide additional evidence for model robustness. Most stations exhibit Total nRMS values between ~0.5 and 1.5, and nearly all remain below the commonly accepted threshold of 3.0 (e.g., TVG244: 0.78; TVG237: 0.67; TVG210: 0.55), reflecting excellent data–model agreement. Even stations with moderately higher values (e.g., TVG214: 1.28; TVG241: 2.48) show no spatial clustering or systematic patterns in the residuals, suggesting that the elevated misfits reflect localized noise rather than structural deficiencies in the model. Tipper RMS values are more variable—as expected due to their sensitivity to cultural noise and near-surface heterogeneity—but remain within acceptable limits and do not significantly influence inversion behavior.

Overall, the consistent reproduction of MT curves across sites, the stable phase agreement, the absence of systematic misfits, and the predominance of low Total nRMS values collectively indicate a well-behaved inversion. Nevertheless, the internal curve-fit diagnostics, together with cross-validation from independent datasets—including gravity, magnetic susceptibility, borehole lithology, and

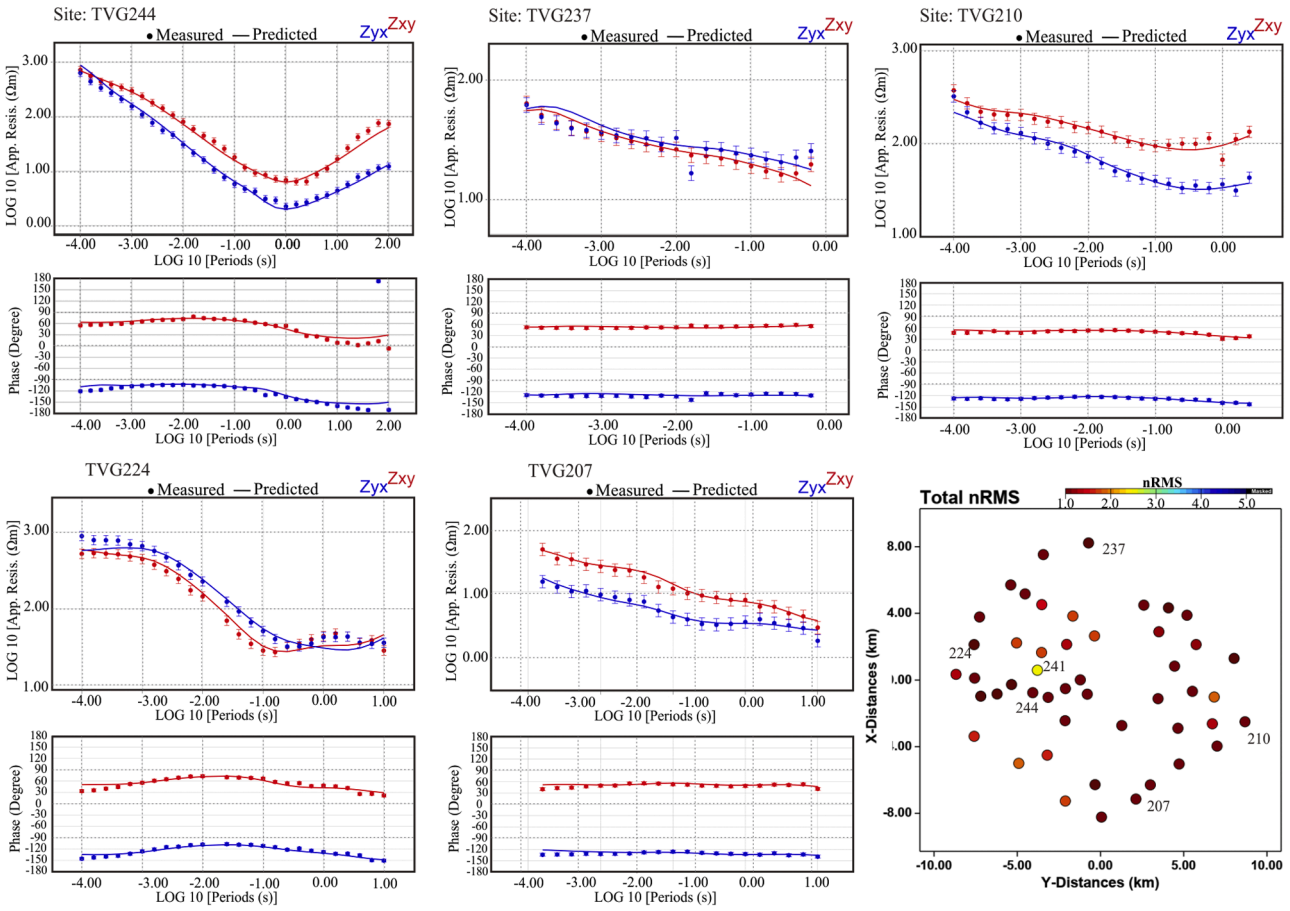

Fig. 3. Apparent resistivity and phase curves for selected MT stations, and spatial distribution of nRMS (normalized root mean square) values.

microseismicity—provide strong support that the major resistivity domains resolved within the upper ~ -3 to -4 km are robust. Interpretations at greater depths are presented cautiously and only where supported by multiple, independent geophysical indicators.

3.2. Geological cross-section construction

Geological cross-sections were constructed to illustrate the subsurface structural framework of the TVG. These cross-sections are based on surface lithological maps incorporating bedding attitudes (Fig. 1b) and stratigraphic thicknesses (Table 1), which together define key surface geological boundaries. Initial subsurface geometries were inferred using the kink method (Suppe, 1983), a widely applied technique for constructing balanced cross-sections based on bedding orientations, stratigraphic sequences, and fault traces.

To improve subsurface resolution—particularly in areas obscured by thick volcanic cover—multiple geophysical datasets were integrated into the interpretation. These include magnetotelluric (MT) resistivity model, microseismicity, gravity (density) anomalies, magnetic susceptibility, and borehole lithological logs. Furthermore, detailed borehole data (Table 2) were incorporated to constrain the base of the volcanic cover.

The sedimentary formation thicknesses adopted in this study are primarily based on Huang (1998), as documented in the guidebook accompanying the official geological map of Taipei, which covers the northeastern coast of Taiwan. The thickness ranges listed in Table 1 are compiled directly from Huang (1998) and reflect spatial variability and methodological differences. For the construction of geological cross-sections and reconstruction of the pre-volcanic sedimentary framework beneath the volcanic cover, representative thicknesses were selected from within these ranges. The adopted values, from youngest to oldest, are: Kueichulin Formation (Kc) – 800 m; Nanchuang Formation (Nc) – 600 m; Nankang Formation (Nk) – 700 m; Shiti Formation (St) – 450 m; Taliao Formation (Tl) – 400 m; Mushan Formation (Ms) – 650 m; and Wuchishan Formation (Wc) – 1200 m (Table 1). These representative values serve as baseline constraints for structural reconstruction and do not imply uniform thickness across the study area.

Geological cross-sections were constructed using the kink method (Suppe, 1983, 1985), which represents folded strata as angular panels to simulate fault-bend and fault-propagation folding. This approach was applied to delineate major structural features in the TVG area, including the Shan-chiao, Jin-shan, and Kan-chiao faults, as well as the Jianshahu anticline and Diaoshih syncline.

To constrain subsurface lithologic boundaries beneath the volcanic cover, borehole data from geothermal exploration wells in the Mt. Qixing–Matsao, Mt. Shamao, Mt. Huangzui, and Jinshan areas were incorporated (Table 2). The wells reveal significant spatial variation in the depth to the sedimentary basement, ranging from >1600 m in the Mt. Qixing–Matsao area (e.g., MTO-1, MTO-2, and E208) to <150 m beneath Mt. Shamao (e.g., E101, E102, and E103).

In addition, thick andesitic dikes intruding the Wuchishan Formation were encountered at depths of approximately 1000–1400 m in several wells (e.g., E208, SHP-1, and CPC-CS-1), indicating substantial magmatic intrusion into the sedimentary basement. These borehole data provide important constraints on the geometry of the pre-volcanic stratigraphy and the distribution of intrusive bodies relevant to the geothermal system.

Table 1
Lithological characteristics and thicknesses of the formations in the study area.

Series	Formation	Thickness (m)	Lithological Characteristics	Note
Miocene	Kueichulin (Kc)	700–900	muddy sandstone	Two members: Tapu formation 300–400 m thick, and Erhchiu Formation 400–500 m thick
	Nanchuang (Nc)	500–600	sandstone, shale, and coal beds	
	Nankang (Nk)	700–750	shale, mudstone, and sandstone	
	Shihti (St)	300–450	composed of alternating sandstones and shales, along with 5 coal beds	Two members, the lower (160 m thick) and the upper (150–160 m)
	Taliao (Tl)	350–850	sequence of marine sandstones, shales, and siltstones. Lower porosity and permeability	
	Mushan (Ms)	450–650	sandstone, shale, and minor coal seams up to 0.3–0.6 m thick, with the sandstone having an average porosity of ~15%, and a maximum value of 25%	
	Wuchishan (Wc)	> 1200	massive sandstone	

4. Results

4.1. MT inversion results

The results of the 3D inversion for the TVG geothermal field are presented in two formats: horizontal resistivity maps at selected depths and vertical resistivity cross-sections. All cross-sections are oriented northwest–southeast (NW–SE), approximately perpendicular to the prevailing fault systems (Fig. 1). The analysis focuses primarily on structures shallower than -5 km, where most geothermal features of interest are concentrated.

4.1.1. Resistivity maps

Fig. 4 presents four horizontal slices of the 3D resistivity model at elevations of -0.19 km, -0.453 km, -0.96 km, and -2.65 km, providing a plan-view of subsurface resistivity variations across the TVG. The resistivity values in the inverted model span a wide range, from approximately 0 Ωm to > 1000 Ωm. Major fault traces, including the Shan-chiao fault, Jin-shan fault, and Kan-chiao fault, are superimposed for spatial reference (Fig. 4a).

A recurring spatial pattern is observed across multiple depths, particularly beneath the Mt. Qixing–Mt. Shamao and Mt. Huangzui–Mt. Dajianhou regions. These areas consistently exhibit a low-resistivity zone near the surface (typically <10 Ωm) that directly overlies a zone of moderately low resistivity (approximately 10–60 Ωm). This vertically stacked configuration is most clearly expressed at -0.453 km and -0.96 km depths and appears spatially coherent, extending laterally within the fault-bounded domain. These two resistivity zones are interpreted as the clay cap and underlying reservoir, respectively, and are outlined by black and gray curves in Fig. 4.

At shallower depths of -0.19 km and -0.453 km (Figs. 4a and 4b), the resistivity distribution is notably heterogeneous, characterized by

Table 2
Summary of borehole locations and geological observations.

Borehole	X (E)	Y (N)	Altitude (m)	Total Depth (m)	Temperature (°C)	Depth to Sedimentary Rock (m)	Notes	Source
E201	306,410.2025	2784,988.852	829.45	572	236			ITRI
E202	306,207.9104	2785,536.437	745.91	441	169			ITRI
E203	306,528.9636	2784,819.711	808.61	1005	241			ITRI
E205	306,688.2168	2784,692.436	799.68	1500	232			ITRI
E207	306,722.7872	2786,012.082	688.02	768	143			ITRI
E208	306,389.8785	2785,036.631	816.85	1510	293	1235	Andesite vents are observed at depths of ~1384 m	ITRI
E209	306,275.4996	2785,352.275		600	36			ITRI
E303	311,237.356	2787,266.729	474	1305		620		ITRI
E212	306,694.9879	2784,479.8	770.71	665	251			ITRI
E213	307,400.6959	2784,403.359		603	123			ITRI
E214	306,997.2369	2784,315.68		503	172			ITRI
E101	303,494.0567	2781,869.776	241.39	520	198	38		ITRI
E102	303,928.4306	2781,625.126	271.67	629	175	123		ITRI
E103	303,099.6309	2781,841.074	223.53	1000	155	63		ITRI
G501	309,800	2787,600		623	138			ITRI
MTO-1	30,681.805	2784,347.869	729.6	1717		1629		CPC
MTO-2	306,669.03	2783,183.746	615.1	1600		1166		CPC
SHP-1	310,413.13	2787,878.236	332.56	2020		811	Andesite vents are observed at depths >1040 m	CPC
CPC-CS-1	315,736.849	2789,529.746		2001.8		210	Andesite vents are observed at depths > 1400 m	CPC
LNB-01	313,714	2792,312	12.51	300				Sinotech
LNB-02	313,793	2792,205	11	300				Sinotech
LNB-03	313,761	2792,263	10.4	700			Reach Wc at 503 m, Nc at 586.95 m	Sinotech
CPC-CS-6	315,805.912	2789,597.621				244.5		CPC
CPC-CS-7	314,680.529	2790,792.234				375.35		CPC
CGS-Sanzhi	304,192	2793,115	391	600		353		GSMMA
CGS-Zhugaoling	307,770	2782,182	482	600		420.7		GSMMA

Footnote: Data were obtained from the Engineering Geological Investigation Databank maintained by the Geological Survey and Mining Management Agency (GSMMA), Ministry of Economic Affairs, Taiwan. ITRI and CPC are Industrial Technology Research Institute and Chinese Petroleum Corporation, respectively.

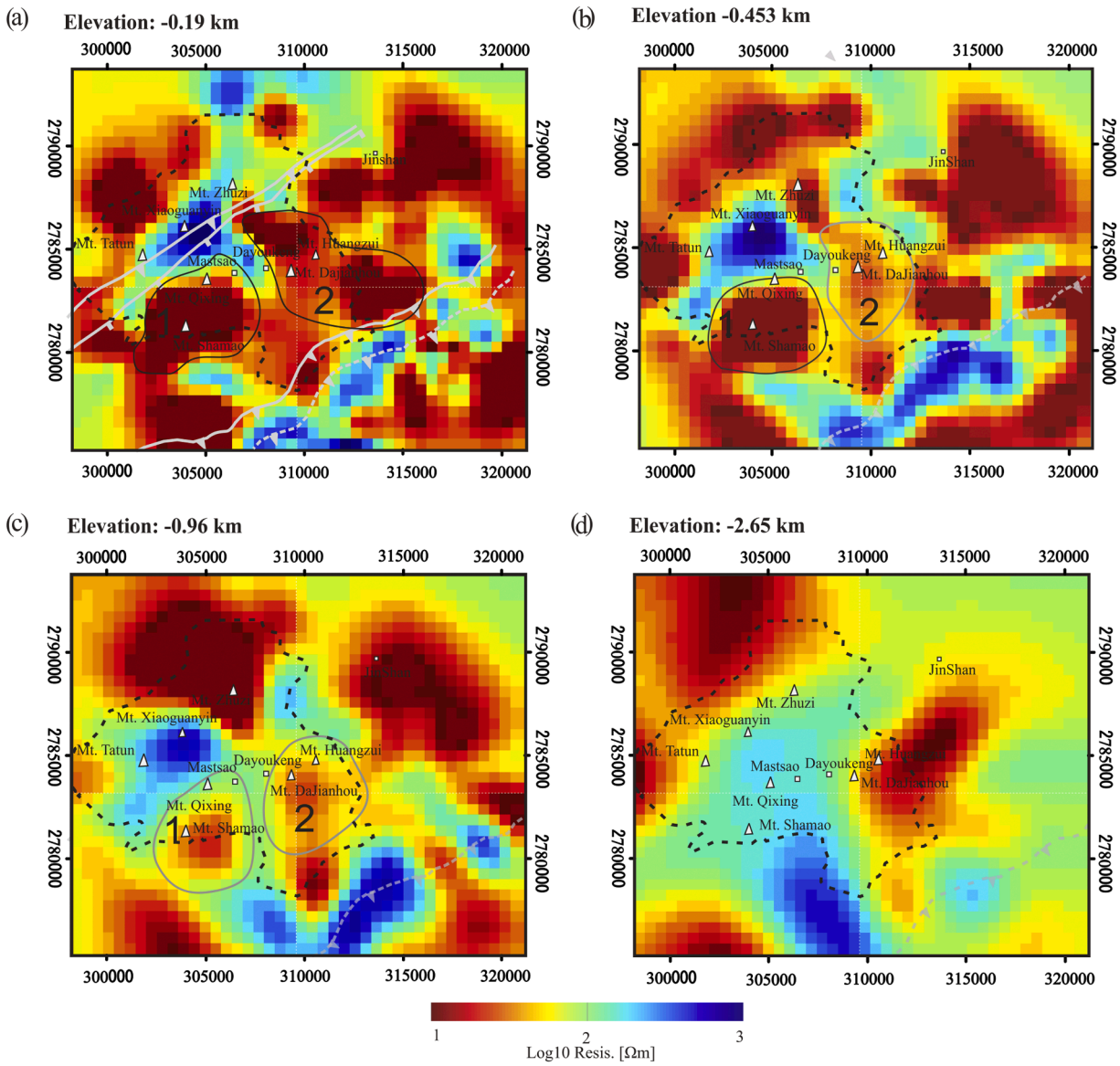

Fig. 4. Plan-view resistivity distributions at selected elevations across the TVG. Cooler colors indicate higher resistivity, whereas warmer colors represent lower resistivity. The black curves outline the interpreted clay-cap boundaries, and the thin gray curves delineate the underlying reservoir zones. Thick white lines indicate the surface traces of major faults (panel a). The dashed white lines show the projected subsurface traces of the Kan-chiao fault at different depths, assuming a dip angle of ~30° toward the southeast (Huang et al., 1991). The black dashed curve marks the boundary of Yangmingshan National Park.

interleaving high- and low-resistivity patches. Low-resistivity anomalies are distributed throughout the central TVG, while high-resistivity regions (>100 Ωm) tend to appear along the projected traces of the Jinshan fault/Shan-chiao fault and Kan-chiao fault. At -0.96 km depth (Fig. 4c), the resistivity patterns become more continuous, with several moderately resistive domains forming broad zones that spatially correspond to fault-parallel alignments. By -2.65 km depth (Fig. 4d), the resistivity pattern becomes less pronounced, with high-resistivity features persisting but appearing more localized and less sharply bounded than at shallower levels. Despite the reduced contrast, these features still align approximately with the major fault zones, though the definition of fault-related resistivity boundaries becomes less distinct.

In addition to the surface fault traces (white lines), the subsurface projection of the Kan-chiao fault is also shown in Fig. 4 (dashed line). This interpretation was constructed by projecting the surface fault trace downward using a dip angle of ~30°, following Huang et al. (1991). The projected trace coincides with a zone of relatively high resistivity, suggesting that the Kan-chiao fault maintains structural expression at depth and may exert control on the distribution of resistive domains.

4.1.2. *Resistivity cross-sections*

The resistivity cross-sections of profiles T4, T5, and T6 (Fig. 5, panels a–c) provide vertical cross-sectional views of the resistivity distribution beneath the TVG. The inverted resistivity values range from ~0 Ωm to >1000 Ωm. Across all these profiles, several consistent features emerge. In the shallow subsurface—typically within the upper 2 km—low-resistivity zones (<10 Ωm) are widespread and often laterally extensive, especially in the central portions of each section. These low-resistivity zones are generally underlain by more resistive materials, forming a vertically stratified structure. Moderately resistive zones (10–60 Ωm) commonly appear beneath the shallow low-resistivity layer, extending to elevations of approximately -1.5 to -2.0 km. At greater depths (below about -3 km), resistivity values increase significantly, with broad, laterally continuous high-resistivity domains (>100 Ωm) appearing in all profiles.

Subvertical resistivity contrasts appear to delineate the subsurface

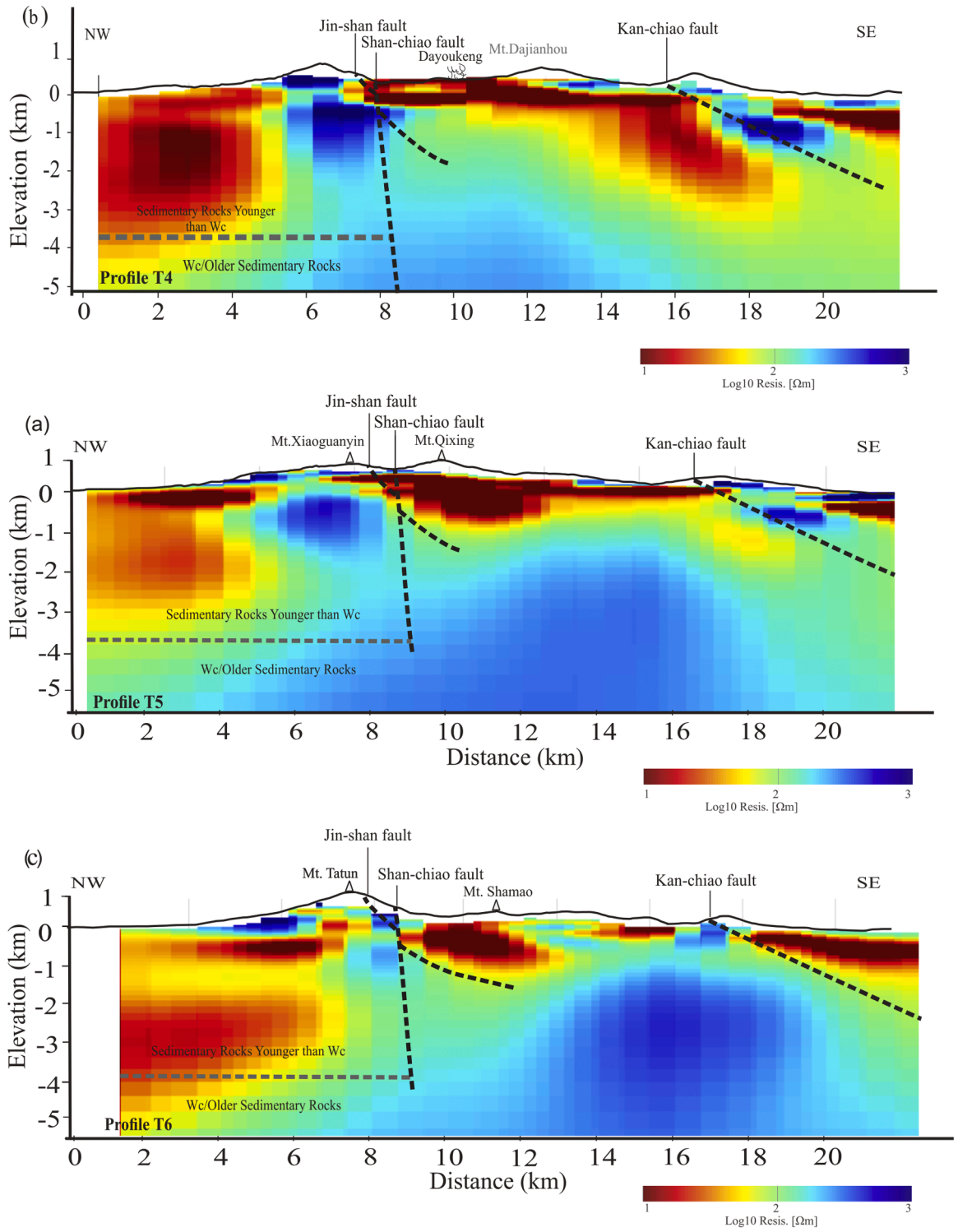

Fig. 5. Resistivity profiles extracted from the 3D resistivity model with Interpretations. Panels show geological and hydrothermal features interpreted along three transects: (a) profile T4, (b) profile T5, and (c) profile T6. Their locations are shown in Fig. 1.

traces of the Jin-shan fault, Shan-chiao fault, and Kan-chiao fault (Fig. 5 panels a–c). These gradients mark sharp transitions in resistivity observed in both shallow and deeper sections of the profiles, suggesting structural compartmentalization. The northwestern segments of all three profiles consistently exhibit deep-reaching low-resistivity zones, extending to elevations of -3.5 to -4 km, before transitioning into high-resistivity domains at greater depth.

Individually, Profile T4 reveals a broad low-resistivity anomaly beneath the northwestern flank of Mt. Xiaoguanyin, gradually giving way to higher resistivity toward the southeast. A southeast-dipping resistive structure appears near the projected trace of the Kan-chiao fault. Profile T5 displays a more heterogeneous resistivity structure, with shallow high-resistivity anomalies beneath Mt. Qixing and the northwestern flank, and a well-defined low-resistivity zone in the central profile segment. Profile T6 features an extensive low-resistivity domain beneath Mt. Tatun, transitioning to more resistive material at depth,

with high-resistivity structures again appearing near the Kan-chiao fault.

Overall, the cross-sections depict a resistivity structure characterized by vertically stratified low-resistivity and high-resistivity layers, lateral segmentation by major faults, and a general increase in resistivity with depth near the Kan-chiao fault.

4.1.3. 3D resistivity model

The 3D resistivity structure of the TVG is visualized using six NW–SE-oriented cross-sections (T1–T6), as shown in Fig. 6. These sections integrate the horizontal depth slices (Fig. 4) and the resistivity cross-sections (Fig. 5), providing spatial continuity and geometric context for the interpreted subsurface structures. Shallow zones (above approximately -2 km) of low resistivity (<10 Ωm) appear broadly beneath Mt. Qixing–Mt. Shamao and Dayoukeng–Mt. Huangzui, forms a laterally continuous conductive layer. Moderately resistive bodies (10–60 Ωm), typically associated with geothermal reservoirs, underlie this conductive cap and are lens-shaped, particularly concentrated beneath Mt. Qixing and Mt. Dajianhou.

High-resistivity domains (>100 Ωm) dominate the deeper parts of the model, particularly below the elevation of -2.5 to -3 km, and are spatially continuous from T6 to T3 (Mt. Tatun–Mt. Shamao to Mt. Zhuzi–Mt. Huangzui). These features can be interpreted as solidified igneous intrusions or crystalline basement. In contrast, toward the northwest—from T3 to T1 (Mt. Huangzui to Jinshan)—lower resistivity values (<30 Ωm) persist down to ~ -4 km depth, suggesting either absence or deeper depth resistive bodies in this region.

The alignment of resistivity transitions with major faults and the continuity of vertically layered resistivity zones provide a volumetric framework that supports the conceptual interpretations shown in Figs. 4 and 5.

4.1.4. Preliminary interpretation

The spatial distribution of resistivity features in both map and cross-sectional views indicates a subsurface structure consistent with conceptual models of volcanic-hosted geothermal systems reported by Cumming (2009), Stimac et al. (2015), and Cumming and Mackie (2010). In particular, the recurrent observation of a low-resistivity zone in the upper 1–2 km, systematically overlying a moderately resistive zone, mirrors the classical configuration of a clay-rich alteration cap above a geothermal reservoir. This sequence may correspond to the Smectite-dominated clay cap and the underlying Chlorite-Epidote alteration zone described in previous models (Cumming and Mackie, 2010; Stimac et al., 2015).

The widespread shallow low-resistivity anomalies are interpreted as hydrothermally altered rocks, likely dominated by conductive clay minerals such as Smectite or Illite–Smectite mixtures, formed in a temperature range of 100–200 °C. The underlying moderately resistive units may reflect zones of enhanced fracture permeability and partial alteration, commonly associated with productive geothermal reservoirs. This interpretation is further supported by the consistent depth range and lateral extent of these zones across multiple sections.

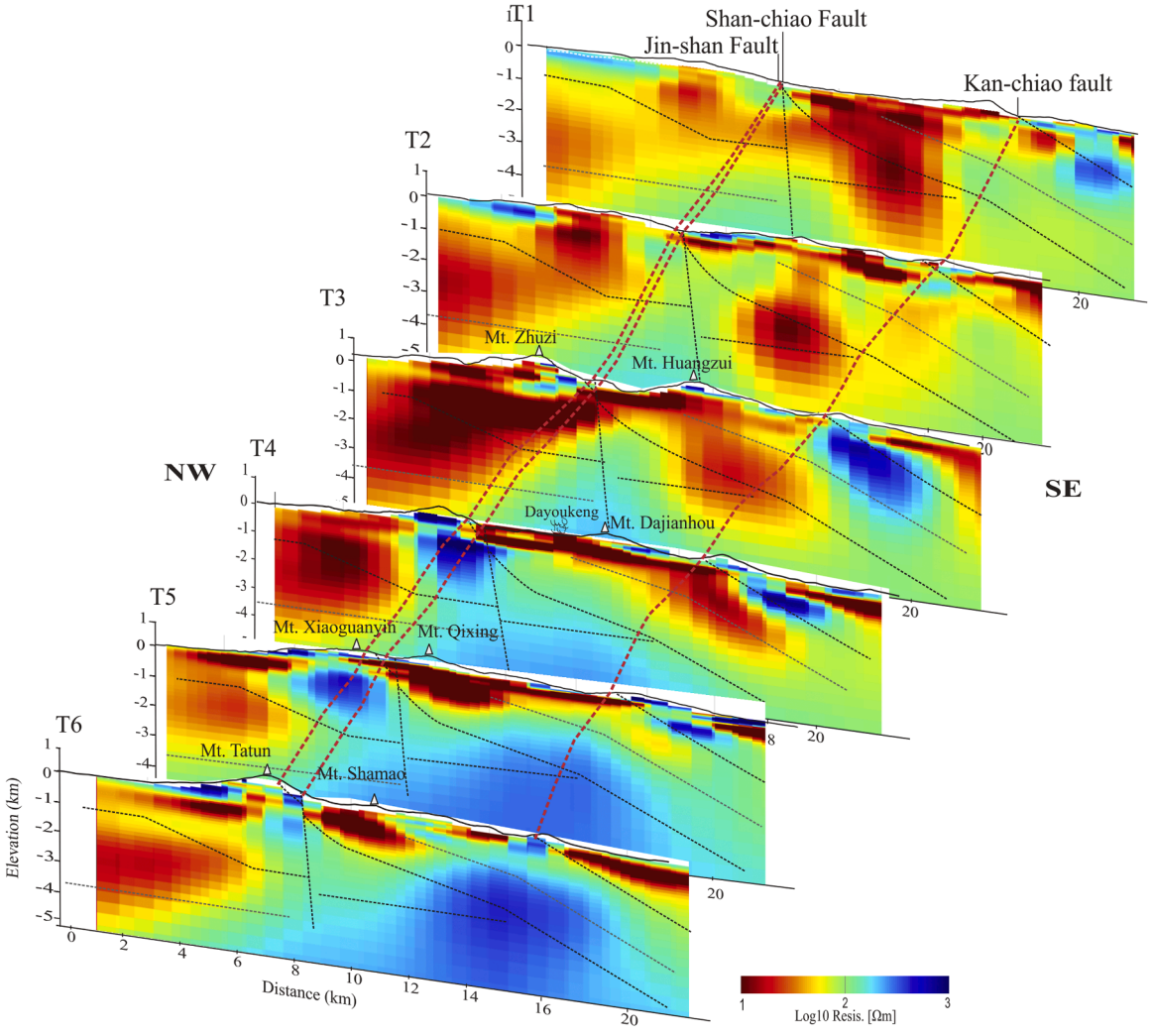

Fig. 6. Resistivity profiles T1, T2, T3, T4, T5 and T6 from right to left at shallow depths. Their locations are shown in Fig. 1.

The deep high-resistivity domains—emerging below approximately -3 to -4 km depth—are likely to represent consolidated igneous intrusions or relatively unaltered crystalline basement. These features exhibit minimal lateral variation and form a resistive base that underlies the clay cap and geothermal reservoir zones, serving as the lower boundary of the geothermal system.

The alignment of resistivity boundaries and anomalies with the major fault traces may imply that fault structures exert a strong control on subsurface fluid flow and lithologic juxtaposition. Both the Jin-shan fault/Shan-chiao fault and Kan-chiao fault coincide with pronounced resistivity gradients or structural transitions, suggesting they may serve as conduits for hydrothermal fluids or barriers to flow that compartmentalize the geothermal system. In particular, the Kan-chiao fault is delineated not only at the surface but also by its projected subsurface trace (Fig. 4), which aligns with a high-resistivity domain consistent with fault-related compartmentalization.

4.2. Geological cross-sections based on geological and geophysical data

4.2.1. Construction and refinement of geological cross-sections

The geological cross-sections in the TVG area were constructed using the kink method, originally developed by Suppe (1983, 1985). Here, we present three representative examples: Profile T1 and Profile T5, oriented NW–SE (Figs. 7 and 8), and Profile P1 oriented NE–SW (Fig. 9), to illustrate the construction process in greater detail.

Profile T1 runs subparallel to the northern coastline, where bedrock

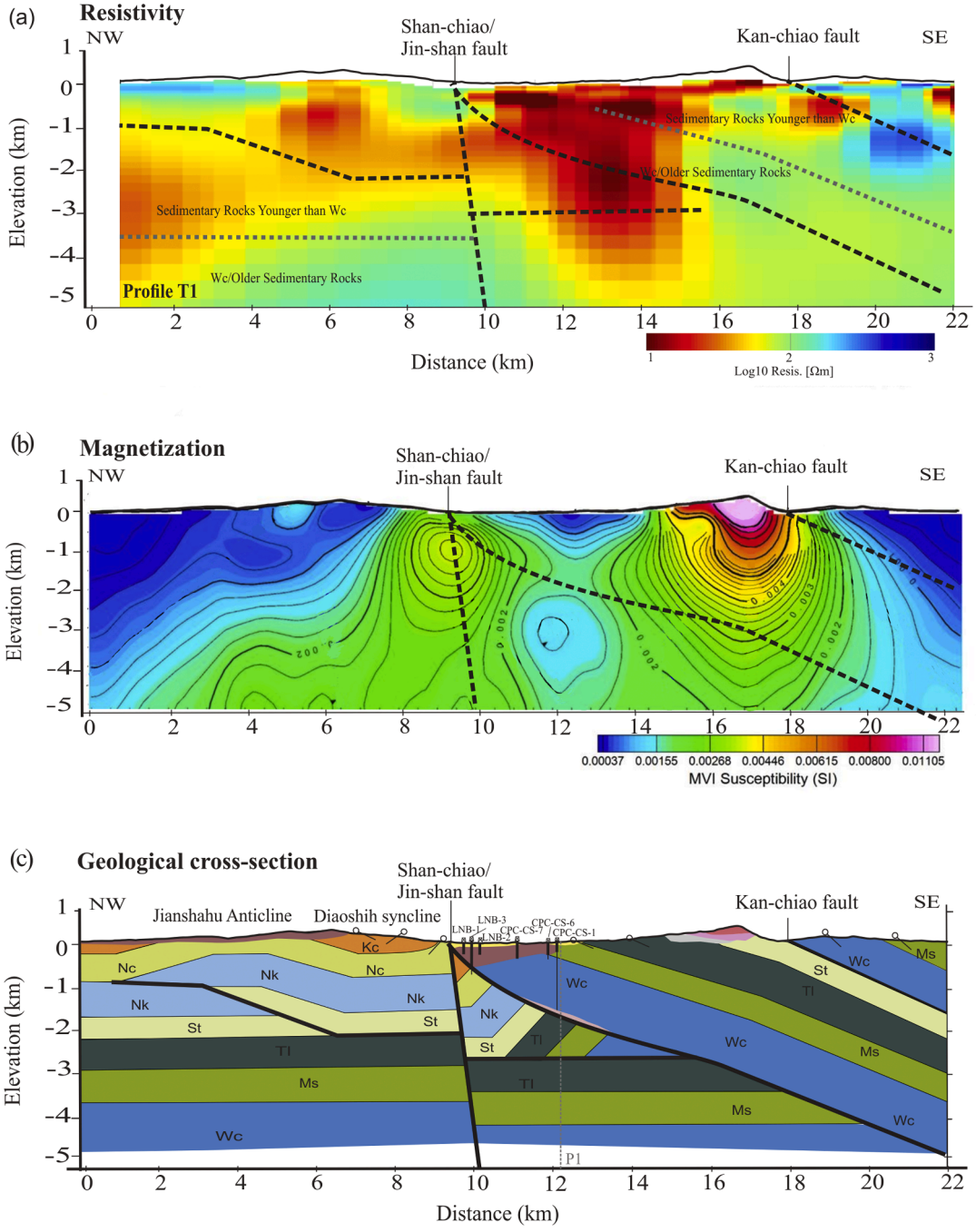

Fig. 7. Geophysical and geological cross-sections along profile T1. The location of profile T1 is shown in Fig. 1. Panels show (a) Resistivity, (b) Magnetization (ITRI, 2015), and (c) Geology. Formation abbreviations follow those used in Fig. 1.

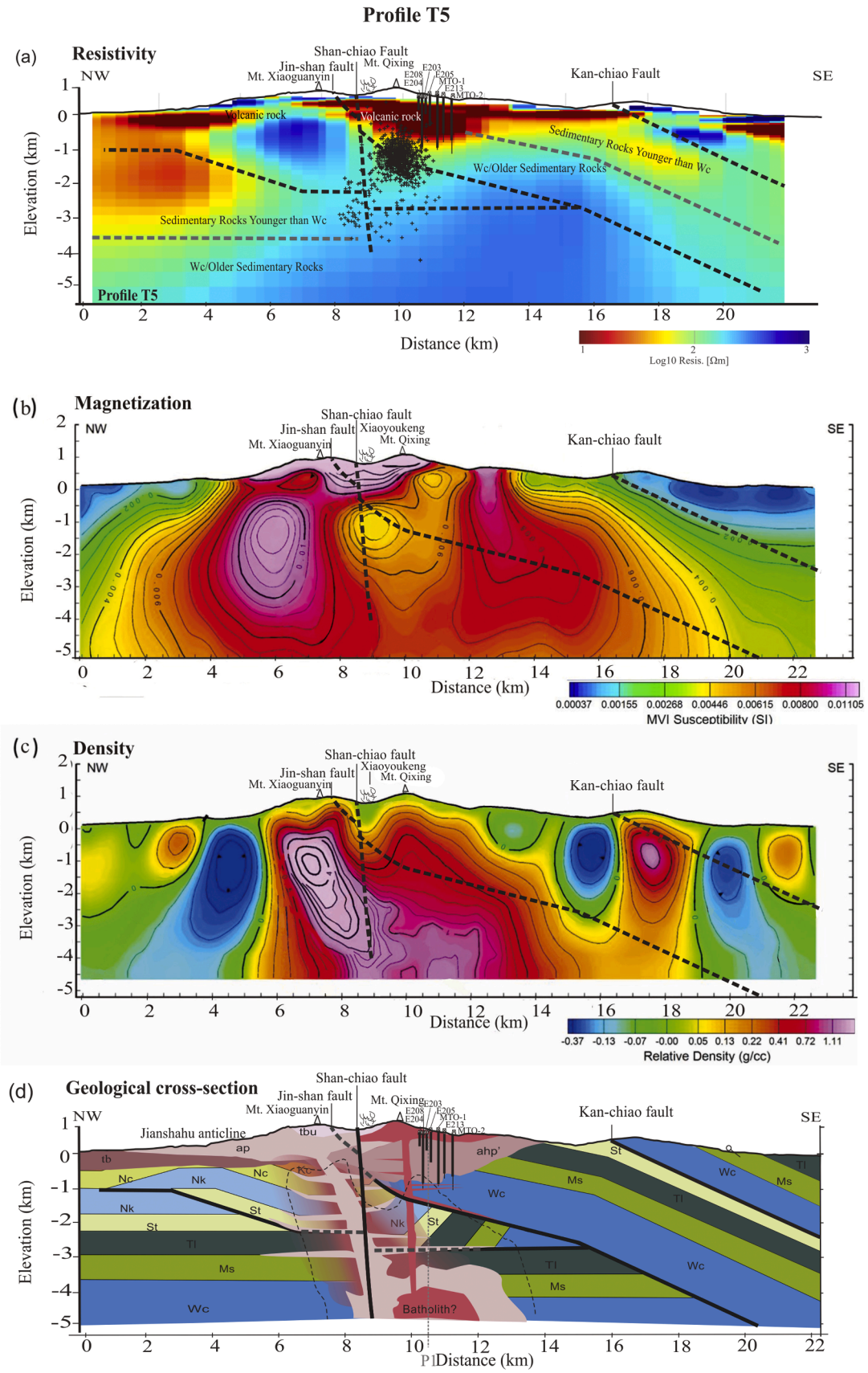

Fig. 8. Cross-sections along profile T5. The Location of profile T5 is shown in Fig. 1 (a) Resistivity profile with cluster microseismic (pluses); (b) Magnetization (ITRI, 2015), MVI denotes "Magnetization Vector Inversion". (c) Density (ITRI, 2015), and (d) Geological cross-section. Formation abbreviations follow those used in Fig. 1.

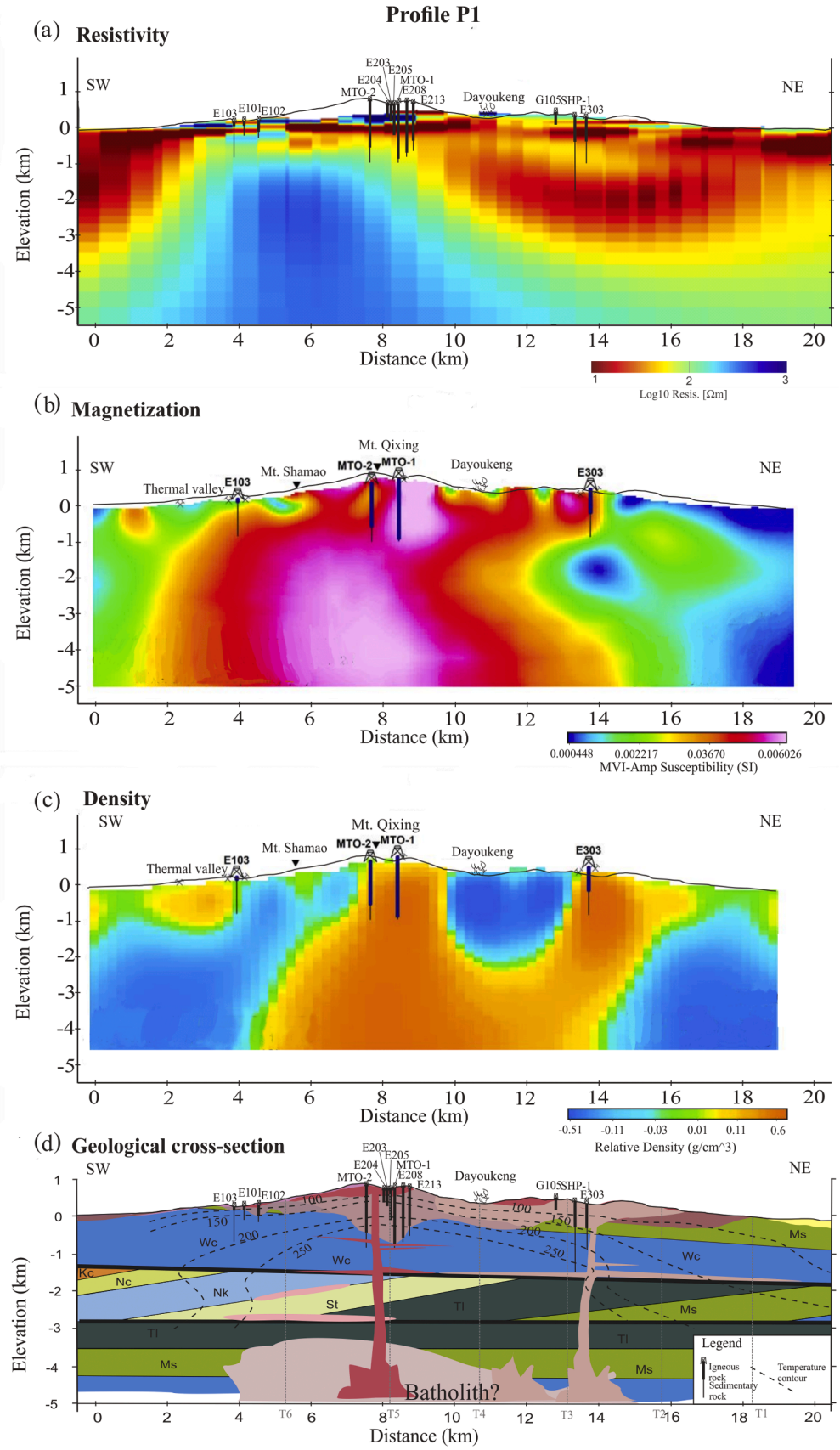

Fig. 9. Geophysical and geological cross-sections along profile P1. The location of profile P1 is shown in Fig. 1. Panels show (a) resistivity; (b) magnetization (ITRI, 2015); (c) density (ITRI, 2015); and (d) geology cross-section. Formation abbreviations follow those used in Fig. 1.

outcrops are well-exposed (Fig. 1). Excluding the recent alluvial deposits, the youngest sedimentary unit is the Pliocene Kueichulin Formation, which crops out northwest of the Shan-chiao fault. However, similar to other NW–SE profiles, the ground along the northwestern one-third of Profile T1 is covered by extensive pyroclastic deposits. This challenge was addressed by incorporating offshore seismic reflection data from profile OR2–1394–6 and its interpretation by Chen (2014), which together reveal a buried frontal fold—referred to in this study as the Jianshahu Anticline—with a half-wavelength of approximately 6 km beneath the pyroclastic cover. The forelimb of the anticline is underlain by relatively undeformed sedimentary strata. To better explain the geometry and isolation of the Jianshahu Anticline, a flat-ramp-flat structure in the footwall of the Jin-shan fault was introduced by Chen (2014). This structural configuration accounts for the upward bending of the hanging wall and is incorporated in our interpretation of Profile T1 (Fig. 7). In contrast, ITRI (2021) shows this area as a tightly folded train, suggesting more localized transpression or intense shortening, while Teng et al. (1992) and Chu et al. (1998) depict a nearly undeformed sequence with horizontal formations, likely oversimplifying the structural complexity and ignoring crustal shortening.

The geometry of major faults (Jin-shan, Shan-chiao, and Kan-chiao) was refined through integration with borehole and geophysical constraints. The Shan-chiao fault is interpreted as a steeply southeast-dipping normal fault (75–85°), consistent with Chen et al. (2014), whereas the Kan-chiao fault is recognized as a gently southeast-dipping reverse fault (~30°), which was refined using MT resistivity models described earlier and in agreement with Huang et al. (1991) (Fig. 7). The Jin-shan fault is reliably constrained by borehole LNB-03, which intersected the fault plane at a depth of 585.85 m (Sinotech, 2013) (Fig. 7).

The base of the volcanic cover was constrained using data from boreholes CPC-CS-6, CPC-CS-7, and LNB-03, all of which penetrated the igneous layer. Magnetization data further aid in delineating lithological contacts. Regions with the highest susceptibility values, up to 0.01105 SI, correspond to exposed igneous rocks (Fig. 7b and c), while values ranging from 0.00037 to 0.00266 SI are associated with sedimentary formations. This contrast supports the identification of intrusive igneous bodies in other profiles as well.

The subsurface geometry of sedimentary units—the framework of the Profile T1 cross-section—was inferred using the kink method, based on bedding attitudes, stratigraphic sequences, and fault traces. This structural interpretation is extended to other NW–SE-oriented cross-sections in the region. The strength of our approach lies in integrating diverse datasets. The subsurface geometry of sedimentary units was reconstructed using the kink method, guided by bedding attitudes, stratigraphy, and fault traces, and was further tested against geophysical (offshore seismic profiles, resistivity, density, and magnetization) and borehole data offshore seismic profiles. This cross-validation reduces interpretive bias. By comparison, earlier studies (Chu et al., 1998; ITRI, 2021; Teng et al., 1992) relied primarily on the freehand method, which, although flexible, lacks structural constraints and therefore provides lower accuracy in defining fault geometries and regional deformation histories.

Profile T5 runs through Mt. Qixing and closely passes Mt. Xiaoguanyin (Fig. 1), both of which are interpreted as remnants of volcanic necks. High magnetic susceptibility anomalies can be traced from these two edifices to depths of approximately -5 km (Fig. 8b). Based on the density profile (Fig. 8c), a volcanic conduit connected to the Xiaoguanyin neck can be clearly delineated. In contrast, the conduit beneath Mt. Qixing is less distinct, likely due to its smaller size or elevated temperatures in the region, which significantly reduce magnetic susceptibility—especially in andesitic rocks that typically contain higher concentrations of magnetic minerals. Accordingly, two volcanic conduits of different sizes connected to a deeper batholith are interpreted in Fig. 8b This interpretation is further supported by MT-derived resistivity data, which reveal a high-resistivity zone (>100 Ωm) in the footwall of the Jin-shan–Shan-chiao fault that extends downward and broadens at depth (Fig. 8a). The base of the igneous cover is constrained by boreholes E203, MTO-1, E213, and MTO-2, all of which penetrate the volcanic sequence. Fig. 8d integrates these geological and geophysical observations into a unified interpretation.

Profile P1 was constructed along a northeast–southwest (NE–SW) transect, subparallel to the major fault systems of the TVG (Fig. 1), intersecting key surface geothermal manifestations, including hot springs and fumaroles in the Mt. Shamao, Mt. Qixing–Matsao, Dayoukeng–Mt. Huangzui, and Jinshan coastal areas. Fig. 9 presents the integrated interpretation of Profile P1, incorporating MT resistivity data (Fig. 9a), magnetic susceptibility (Fig. 9b), gravity anomalies (Fig. 9c), and borehole constraints (Fig. 9d).

The MT inverted resistivity result reveals prominent high-resistivity zones (>100 Ωm) near the surface, interpreted as andesitic volcanic rocks. Beneath Mt. Qixing, an extensive arc-shaped high-resistivity anomaly extends from approximately -1 km to over -5 km. This continuous structure spans from Mt. Shamao to Dayoukeng at depth and is interpreted as a solidified intrusive body emplaced at depth. Magnetization data corroborate this interpretation, with susceptibility values ranging from 0.005 to 0.006 SI coinciding spatially with the high-resistivity zone. Likewise, the gravity data reveal elevated densities (0.11–0.6 g/cm^3) in the same region, consistent with intermediate to mafic intrusive compositions. At elevations shallower than -2 km beneath Mt. Qixing and Dayoukeng, the structure narrows and is interpreted as volcanic conduits or pipes (Fig. 9b).

The thin high-resistivity cap observed near the surface above these intrusions is interpreted as cooled surface andesite derived from deeper magmatic sources (Fig. 9d). These geophysical signatures are further constrained by borehole data (e.g., MTO-1, MTO-2, E208, E213), which place the top of the sedimentary basement at elevations approximately -0.5 km. Mineralogical analyses from borehole logs in the Mt. Qixing–Matsao area (Fig. 11a) report the presence of pyrite, magnetite, and hematite, supporting the interpretation that crystallized andesitic intrusions are the source of the observed resistivity and density anomalies.

4.2.2. Semi-3D geological model

Fig. 10 illustrates a semi-3D geological framework derived from multiple NW–SE geological cross-sections. These profiles were individually constructed using surface geology, stratigraphic N thicknesses, borehole information, and geophysical constraints (Figs. 7 and 8; Supplementary documents) and were subsequently interpolated laterally to provide a three-dimensional perspective. Because the interpolation is performed between discrete 2D sections, this model does not represent a volumetric 3D inversion. Instead, it reflects a structural interpretation constrained along the section lines and extrapolated between them. These geological profiles correspond spatially to the resistivity cross-sections shown in Fig. 6. Surface lithology and surface bedding orientation were derived from detailed geological maps (Fig. 1b), while the subsurface stratigraphy boundary was refined using stratigraphic thicknesses (Table 1) and borehole records (Table 2), MT resistivity data (Figs. 4 and 5) and supporting geophysical information such as microseismicity, gravity (density) anomalies, and magnetic susceptibility (Figs. 7 and 8; Supplementary document).

The model delineates major stratigraphic units, including volcanic sequences at the surface (e.g., Mt. Qixing, Mt. Tatun, Huangzui) and covers sedimentary formations such as the Keichulin (Kc), Nanchuang (Nc), Mushan (Ms), Taliao (Tl), and Wuchishan (Wc) Formations. Volcanic cover is thickest in the central profiles (from T3 to T5). Borehole data (e.g., E208, CPC-CS-1, MTO-1, MTO-2) confirm the maximum thickness of the presence of andesite rock in these areas up to approximately 1.63 km (Table 2, Fig. 8).

Intrusive bodies are modeled as steeply southeast-dipping, particularly along the Jin-shan and Kan-chiao faults. These intrusions are constrained by co-located anomalies in resistivity (>100 Ωm), magnetic susceptibility (~0.005–0.01 SI), and relative density (>0.6 g/cm^3), and are supported by borehole observations of andesite veins and contact

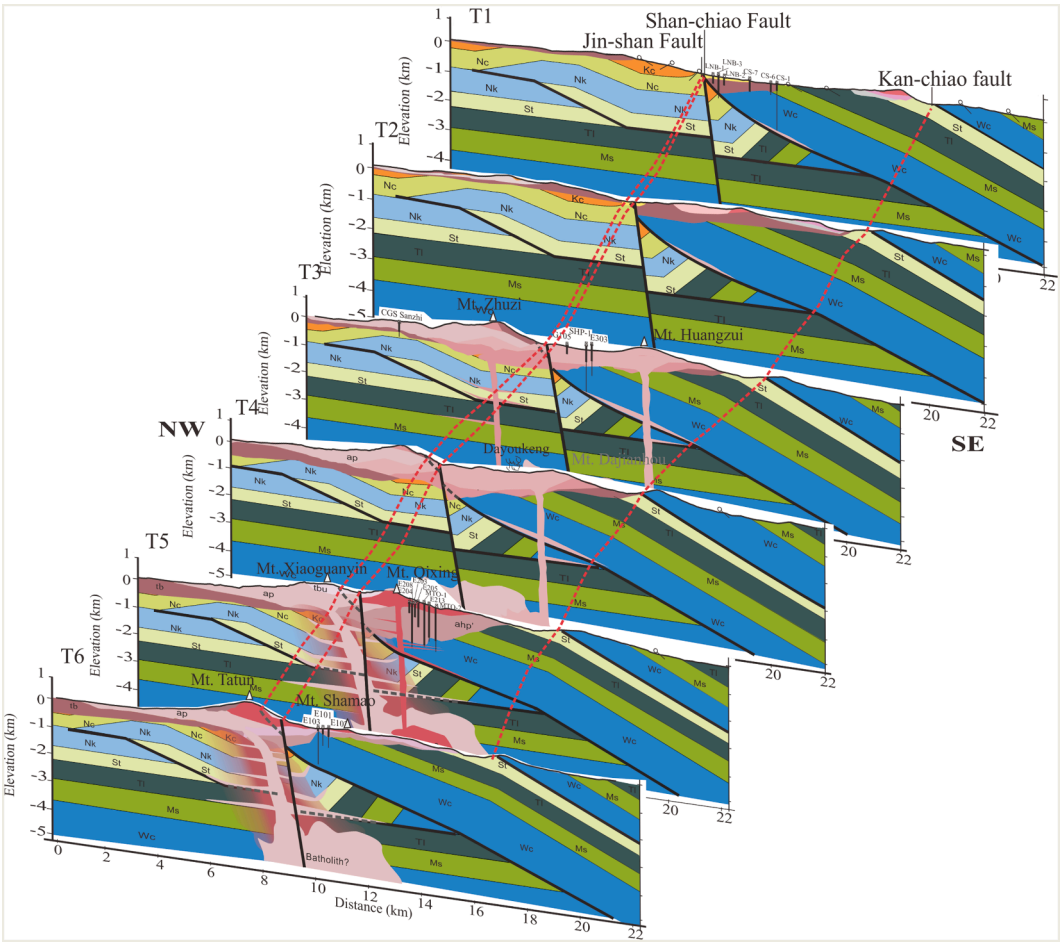

Fig. 10. 3D Structural Interpretation of NW-SE Transect.

metamorphism (Table 2). A larger, consolidated igneous body (interpreted as a batholith) dominates the deeper portions of the model beneath Profiles T6 to T3, extending from the Mt. Tatun–Mt. Shamao area southeastward toward Mt. Zhuzi–Mt. Huangzui. These intrusive bodies correlate spatially with regions of elevated microseismicity (Fig. 8; Supplementary document: Profile T4) and surface geothermal manifestations such as fumaroles and hot springs, suggesting they serve as both heat sources and structural controls within the geothermal system.

The Jin-shan-Shan-chiao and Kan-chiao faults align with major lithological and resistivity boundaries in the model and display contrasting structural styles. The Jin-shan fault zone, in particular, exhibits a thrust-related geometry and accommodates folding, including the Jianshahu Anticline, whose inland continuation is inferred from offshore seismic reflection data (Chen, 2014) and refined in this study (Figs. 7 and 8).

The present model identifies a deep, laterally extensive, high-resistivity batholith beneath the central TVG, extending from Mt. Tatun–Mt. Shamao to Mt. Zhuzi–Mt. Huangzui (Profiles T6 to T3). This feature is constrained by magnetotelluric (MT) resistivity data, gravity, and magnetic anomalies (Figs. 8 and 10; Supplementary document). Southeast-dipping intrusive bodies are mapped along the Jin-shan fault zone, while near-vertical dikes are recognized beneath Mt. Qixing, Mt. Huangzui. These intrusions—correlated spatially with high resistivity, seismicity clusters, high density, high magnetization, and surface geothermal manifestations—are interpreted as the principal heat sources for the geothermal system.

Overall, the semi-3D geological model reveals a stratified, fault-compartmentalized subsurface architecture beneath the TVG. Fault-guided intrusions, clay-altered cap zones, and overlying volcanic and sedimentary successions collectively define the thermal and structural framework of the geothermal system. The spatial arrangement of these features—integrated through geological and geophysical data—highlights the role of structural control in heat distribution, fluid migration, and reservoir development, and provides a robust foundation for geothermal resource assessment and future drilling strategy.

5. Discussion

5.1. Controls on geothermal system development

The integrated resistivity, magnetic, gravity, and microseismic results delineate two major geothermal systems within the Tatun Volcano Group (TVG): (1) the Mt. Qixing–Matsao–Mt. Shamao area (System 1) and (2) the Mt. Huangzui–Mt. Dajianhou–Dayoukeng area (System 2) (Fig. 4). Both systems exhibit a typical clay-cap–reservoir configuration that characterizes many high-enthalpy geothermal fields worldwide.

System 1 lies in the hanging wall of the Jin-shan fault and Shan-chiao fault (Fig. 4). The clay cap identified in the MT resistivity model (<10 Ωm) extends from -0.4 km to -0.5 km, with an approximate radius of 2.5 km, a central thickness of ~1 km, and thinning to ~0.2 km toward the margins (Figs. 4 and 11). This conductive zone coincides with hydrothermal alteration observed in borehole cores. Borehole data (Lan et al., 1980) confirm zoned alteration, showing smectite–chlorite–rich layers at -0.2 to -0.6 km depth and deeper illite–epidote assemblages below 0.6 km (Fig. 11a). Beneath the cap lies a concave lens–shaped reservoir (10–60 Ωm) at elevations of -0.4 to -1 km, with a radius of ~2 km, ~0.6 km thickness, and an estimated volume of ~10 km^3. Microseismic

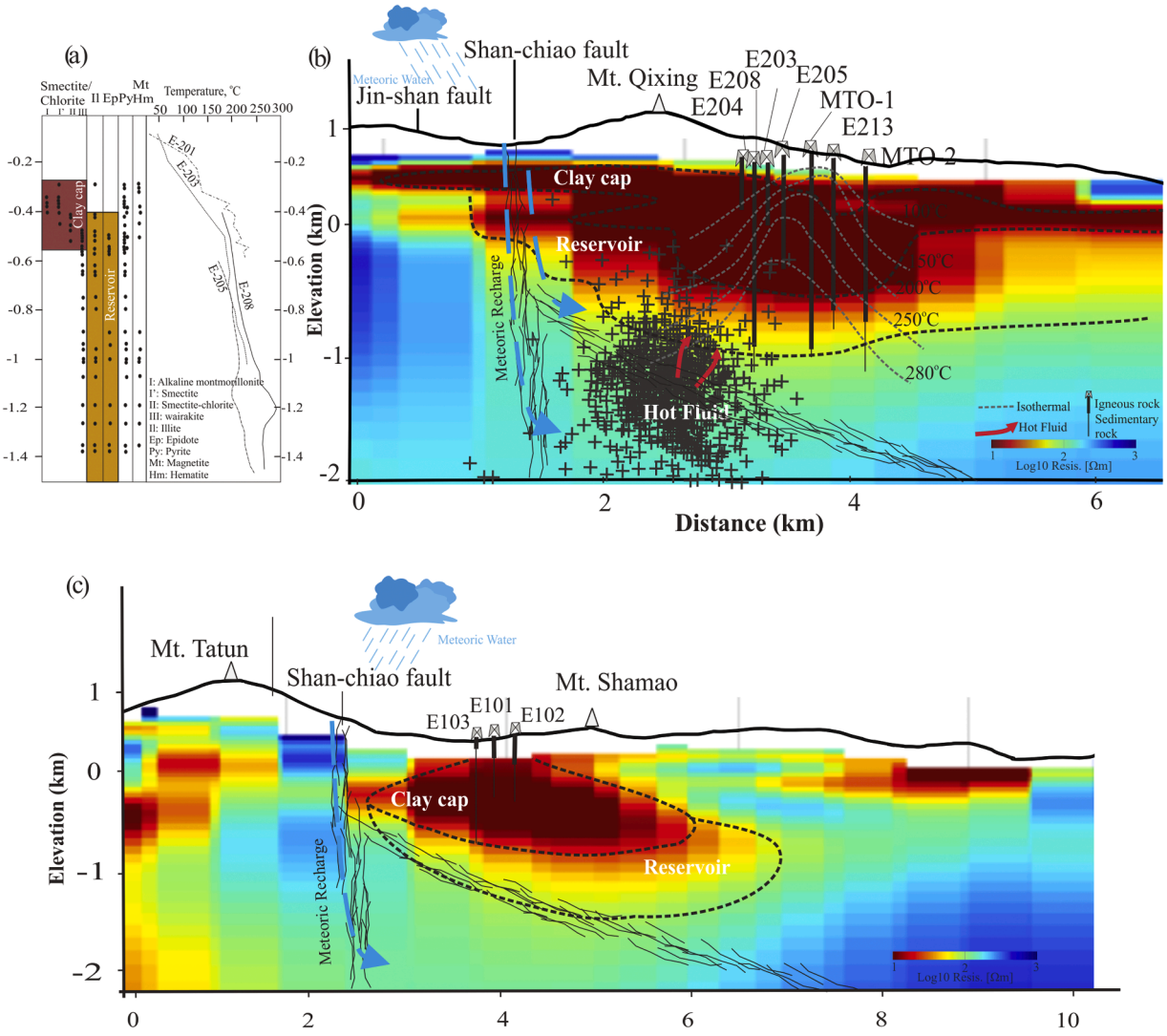

Fig. 11. (a) Temperature and mineral assemblage in boreholes within the Matsao area (left) (adapted from Lan et al., 1980), (b) A model of a geothermal system in the Matsao (Profile T5) (plus symbols indicate microseismic), and (c) A model of a geothermal system in the Mt. Shamao (Profile T6).

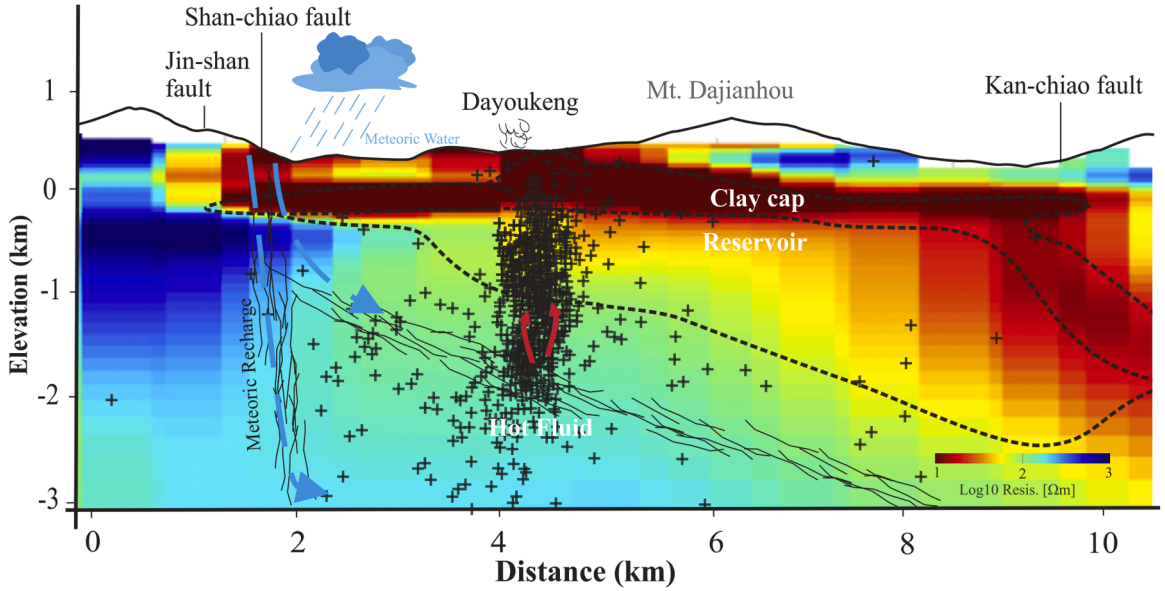

Fig. 12. A model of a geothermal system in the Dayoukeng (Profile T4) (plus symbols indicate microseismic).

clusters spatially coincide with this reservoir (Fig. 11b), suggesting active hydrothermal circulation. Geochemical data further validate this interpretation: Lu et al. (2025) reported neutral reservoir fluids near Mt. Qixing, with clumped isotope thermometry indicating temperatures of 232–276 °C. Moreover, ongoing geothermal production at Matsao supports the productivity of this system. These complementary datasets confirm that System 1 represents a well-constrained and economically viable geothermal reservoir.

System 2, located in the hanging wall of the Jin-shan fault (Fig. 4), shows a similar configuration. The clay cap (<10 Ωm) forms a convex lens with a ~2 km radius, a central thickness of ~0.6 km, and thinning to ~0.2 km at the margins. The underlying reservoir (10–60 Ωm) extends ~2.5 km in radius, ~0.6 km thick at the center, and 1.5–2 km thick at the edges, with an estimated volume of ~16–18 km^3 (Fig. 12). Although no deep borehole penetrates this area, the reservoir coincides with microseismic clusters and fumarolic activity at Dayoukeng, indicating active hydrothermal circulation. Geochemical data from Lu et al. (2025) identify a geothermal zone northeast of Mt. Huangzui containing neutral fluids with reservoir temperatures of ~181 °C, consistent with the resistivity-defined reservoir. The absence of drilling validation remains a limitation, but the convergence of geophysical anomalies, geothermal manifestations, and geochemical constraints strongly supports the geothermal potential of System 2.

Comparative studies in other volcanic provinces reinforce these findings. In Ethiopia, the resistivity models of the Alalobeda and Tendaho geothermal fields revealed shallow low-resistivity smectite caps underlain by resistive chlorite–epidote zones (Abebe et al., 2021). Similarly, at Shalla–Abayata, clay caps of 1–10 Ωm overlie more resistive chlorite–epidote reservoirs (20–100 Ωm) at >2 km depth (Keto and Saibi, 2021). At the Ashute geothermal site, a conductive smectite–illite/chlorite horizon (<10 Ωm) is underlain by intermediate resistivity (10–46 Ωm), attributed to chlorite–epidote alteration at depth (Abossie et al., 2023). In Iceland, the Reykjanes and Hengill systems display the classic three-layer pattern of a smectite–zeolite clay cap, a chlorite–epidote reservoir, and a deep conductive zone associated with active fluid circulation (Árnason et al., 2010; Bretaudeau et al., 2021). On Gran Canaria, 3D MT imaging reveals low-resistivity (<10 Ωm) zones linked to hydrothermal alteration and pervasive 20–50 Ωm zones around the Tejeda caldera (Ledo et al., 2021).

These analogues confirm that resistivity signatures are consistent across volcanic geothermal systems, but also demonstrate that interpretations gain robustness when supported by drilling, geochemistry, and seismicity. Therefore, while resistivity imaging is a valuable first-order tool for identifying geothermal prospects, reliable resource assessment in the TVG requires a multidisciplinary integration of geological, geochemical, and operational data.

5.2. Fault-controlled development of shallow geothermal systems

A fundamental question in evaluating the geothermal potential of the TVG is how major faults influence the distribution and productivity of geothermal reservoirs. Productive systems generally require two essential components: a low-permeability clay cap formed by hydrothermal alteration, and an underlying hot, permeable reservoir, where permeability arises either from primary porosity or from fault-induced fracturing (Grant and Bixley, 2011).

In the TVG, both geothermal systems identified in both System 1 and System 2 occur within the hanging-wall blocks of the Jin-shan and Shan-chiao faults. In contrast, the adjacent footwall zones along the Jin-shan and Kan-chiao faults are characterized by high resistivity values (>100 Ωm), interpreted as intact volcanic rock. Further northwest within the footwall domains, thick conductive zones (<10 Ωm) are also observed, representing hydrothermally altered, low-permeability regions. Both the high-resistivity intact volcanic rocks and the low-resistivity altered zones correspond to low-permeability domains that inhibit fluid flow.

Independent datasets support this structural control. Hanging-wall blocks are typically more fractured and permeable due to fault-related deformation (Galvão et al., 2018). Microseismic activity within the TVG is also concentrated in hanging-wall domains (Lin et al., 2005; Pu et al., 2020, 2025), indicating fracture-controlled fluid circulation. Hydrothermal alteration patterns further illustrate this relationship. In System 1 (Mt. Qixing–Matsao–Mt. Shamao), surface acidic fumarolic alteration transitions downward into neutral, carbonate-bearing zones, suggesting a vertically zoned hydrothermal system. In contrast, Mt. Dajianhou in System 2 exhibits advanced argillic alteration associated with highly acidic fluids, while Mt. Huangzui hosts vapor-dominated, near-neutral reservoirs (Lu et al., 2025). These alteration trends coincide spatially with the resistivity-defined systems, reinforcing that both geothermal reservoirs are confined to the hanging-wall domains of the Jin-shan fault and Shan-chiao fault.

The occurrence of two geothermal systems within hanging-wall regions raises a key interpretive question: do these faults merely serve as conduits for fluid migration, or do they fundamentally control reservoir localization? The evidence favors the latter interpretation—fault geometry and kinematics appear to exert first-order control on reservoir development and permeability structure in the TVG.

Analogous relationships between fault architecture and reservoir localization have been documented globally. In the Andes, productive geothermal fields such as Tinguiririca and Tolhuaca consistently develop within fractured hanging-wall blocks, while footwall zones act as low-permeability barriers (Pearce et al., 2020; Roquer et al., 2017). In Japan, deep drilling at Kakkonda demonstrated that the most permeable and hydrothermally altered reservoirs occur within hanging-wall fault zones, with variable alteration reflecting local fluid chemistry (Muraoka et al., 1998; Sawaki et al., 1997). Similarly, in Iceland, resistivity and borehole data place productive reservoirs above normal-fault hanging walls (Árnason et al., 2010).

Collectively, these global analogues underscore a consistent pattern: hanging-wall blocks provide the most favorable conditions for geothermal reservoir development. Applied to the TVG, this implies that the hanging walls of the Jin-shan fault and Shan-chiao fault should be prioritized as primary exploration targets for future geothermal development in northern Taiwan.

5.3. Overall implications for geothermal development

The integration of geological, geophysical, and geochemical evidence in this study provides a coherent framework for understanding geothermal resource distribution within the Tatun Volcano Group (TVG). Two major geothermal systems—Mt. Qixing–Matsao–Mt. Shamao (System 1) and Mt. Huangzui–Mt. Dajianhou–Dayoukeng (System 2)—exhibit well-developed clay-cap–reservoir configurations typical of high-enthalpy volcanic settings. Both systems occur within the hanging-wall domains of the Jin-shan fault and Shan-chiao fault, where fault-related fracturing enhances permeability and facilitates hydrothermal circulation.

The integrated datasets demonstrate that resistivity imaging alone cannot fully constrain geothermal potential; instead, a multidisciplinary approach incorporating borehole alteration profiles, microseismicity, and geochemical signatures yields a more reliable assessment. System 1, supported by borehole evidence, temperature estimates of 232–276 °C, and ongoing production at Matsao, represents a confirmed high-temperature resource. System 2, although lacking drilling verification, exhibits similar geophysical and geochemical characteristics, with estimated reservoir temperatures of ~181 °C, indicating substantial untapped potential.

These findings highlight that the fault-controlled architecture of the TVG governs reservoir localization, permeability distribution, and fluid chemistry. Accordingly, the hanging walls of the Jin-shan fault and Shan-chiao fault should be prioritized as exploration targets for future geothermal development in northern Taiwan. Continued integration of MT imaging with drilling, seismic monitoring, and geochemical surveys

will be essential to reduce uncertainty and to advance sustainable resource utilization.

6. Conclusions

This study presents an integrated geological and geophysical investigation of the Tatun Volcano Group (TVG) to advance understanding of its geothermal systems and subsurface architecture. By combining magnetotelluric (MT) resistivity data with gravity, magnetic, seismic, borehole, geochemical, and surface thermal evidence, we refine existing conceptual models and delineate the principal geothermal structures.

The results validate the characteristic configuration of volcanic geothermal systems— a low-resistivity clay cap (<10 Ωm) overlying a moderately resistive reservoir (10–60 Ωm). Two distinct geothermal systems are identified: (1) beneath the Mt. Qixing–Matsao–Mt. Shamao area (System 1), supported by borehole observations, geochemical analyses, and operational production data, and (2) beneath the Mt. Huangzui–Dayoukeng–Mt. Dajianhou area (System 2), where supporting evidence is mainly geophysical and geochemical.

Cross-sections constructed along NE–SW and NW–SE transects reveal that the Jin-shan and Shan-chiao fault systems exert a primary structural control on the distribution and characteristics of geothermal reservoirs. Geophysical anomalies also indicate the presence of intrusive igneous bodies, particularly beneath Mt. Qixing, Mt. Dajianhou, and Mt. Huangzui, which likely serve as local heat sources.

Collectively, these findings demonstrate that the hanging-wall domains of the Jin-shan and Shan-chiao faults represent the most favorable targets for geothermal exploration in northern Taiwan. The integrated three-dimensional resistivity and geological framework established in this study provides a robust foundation for visualizing the geometry of geothermal reservoirs, improving resource assessment, and guiding future drilling and development strategies in the TVG.

Declaration of generative AI and AI-assisted technologies in the writing process

During the preparation of this work, the authors used ChatGPT to improve the language and readability of the manuscript. After using this tool/service, the authors reviewed and edited the content as needed and take full responsibility for the content of the published article.

CRediT authorship contribution statement

T. Lan-Chi Nguyen: Writing – review & editing, Writing – original draft, Supervision, Conceptualization. **Wen-Jeng Huang:** Supervision, Visualization, Writing – review & editing. **Chien-Chih Chen:** Supervision, Visualization, Writing – review & editing. **Chi-Shu Yen:** Writing – review & editing, Data curation. **Yi-Heng Li:** Writing – review & editing, Data curation. **Horng-Yuan Yen:** Writing – review & editing, Data curation.

Declaration of competing interest

The authors declare that they have no known competing financial interests or personal relationships that could have appeared to influence the work reported in this paper.

Acknowledgements

We gratefully acknowledge the Geological Survey and Mining Management Agency (GSMMA), the Industrial Technology Research Institute (ITRI), and CPC Corporation for providing access to geophysical and borehole data, particularly Dr. Chi-Hsuan Chen and Dr. Lun-Tao Tong. We also thank Yangmingshan National Park for granting permission to conduct fieldwork.

Supplementary materials

Supplementary material associated with this article can be found, in the online version, at doi:10.1016/j.geothermics.2026.103682.

Data availability

Data will be made available on request.

References

Abebe, G.H., Hersir, G.P., Benediktsdóttir, A., Geirsson, H., 2021. Multi-dimensional inversion of electromagnetic data from Alalobeda. In: Tendaho Geothermal Field in NE-Ethiopia and its Geothermal Significance. Proceedings World Geothermal Congress 2020+1. Reykjavik, Iceland, 24-27 October 2021.

Abossie, A., Fisseha, S., Abebe, B., 2023. 3D analysis of the MT data for resistivity structure beneath the Ashute geothermal site, Central Main Ethiopian Rift (CMER). Heliyon 9, e13202. https://doi.org/10.1016/j.heliyon.2023.e13202, 2023.

Árnason, K., Eysteinsson, H., Hersir, G.P., 2010. Joint 1D inversion of TEM and MT data and 3D inversion of MT data in the Hengill area. SW Icel. Geotherm. 39 (1), 13–34. https://doi.org/10.1016/j.geothermics.2010.01.002.

Belousov, A., Belousova, M., Chen, C.H., Zellmer, G.F., 2010. Deposits, character and timing of recent eruptions and gravitational collapses in Tatun Volcanic Group, Northern Taiwan: hazard-related issues. J. Volcanol. Geotherm. Res. 191, 205–221. https://doi.org/10.1016/j.jvolgeores.2010.02.001.

Bretaudeau, F., Dubois, F., Bissavetsy Kassa, S.G., Coppo, N., Wawrzyniak, P., Darnet, M., 2021. Time-lapse resistivity tomography from land controlled-source electromagnetics (CSEM) over the Reykjanes Geothermal Field. Geophys. J. Int. 226 (3), 1764–1782. https://doi.org/10.1093/gji/ggab172.

Chang, S.C., Chu, M.F., Wang, J.P., Lai, Y.M., Song, S.R., Hemming, S.R., Pan Ng, S.W., Chow, T.D., 2024. Volcanic activity around Taipei, Taiwan: new data and perspectives on the Tatun Volcano Group. Geosci. Lett. 11, 42. https://doi.org/10.1186/s40562-024-00358-2.

Chen, C.H., Burr, G.S., Lin, S.B., 2010. Time of a near-holocene volcanic eruption in the Tatun Volcano Group, northern Taiwan: evidence from AMS radiocarbon dating of charcoal ash from sediments of the Sungshan formation in Taipei Basin. Terr. Atmos. Ocean. Sci. 21, 611–614.

Chen, C.H., Lin, S.B., 2002. Eruptions younger than 20 ka of the Tatun Volcano Group as viewed from the sediments of the Songshan Formation in Taipei Basin. West Pac, Earth Sci. 2, 191–204.

Chen, C.T., Lee, J.C., Chan, Lu, Y.C., Teng, L.S.Y., 2014. Elucidating the geometry of the active Shanchiao fault in the Taipei metropolis, northern Taiwan, and the reactivation relationship with preexisting orogen structures. Tectonics 33, 2400–2418. https://doi.org/10.1002/2013TC003502.

Chen, C.H., Lee, P.T., Lin, C.C., Tong, L.T., Guo, T.R., Lin, R., Chen, M.M., 2023. Insight into the geothermal structure in Tatun Volcano Group. In: Taiwan. Proceedings of the 45th New Zealand Geothermal Workshop. Auckland, New Zealand, p. 8, 15–17 November.

Chen, K.Y., 2014. Study On Structural Development from Orogenic Belt to Extensional Back-Arc Setting in Northern Taiwan and Its Offshore Area. National Central University, Taiwan. Doctoral dissertation.

Cheng, W.T., 1970. Geophysical exploration in the Tatun volcanic region. Taiwan, Geotherm. Spec. Issue 2, 262–274. https://doi.org/10.1016/0375-6505(70)90025-8.

Chu, C.J., Lee, C.T., Teng, L.S., 1998. Structural features and quaternary tectonics of the Chinshan Fault, northern Taiwan. J. Geol. Soc. China 41, 25–42.

Chu, M.F., Lai, Y.M., Li, Q., Chen, W.S., Song, S.R., Lee, H.Y., Lin, T.H., 2018. Magmatic pulses of the Tatun Volcano Group, northern Taiwan, revisited: constraints from zircon U–Pb ages and Hf isotopes. J. Asian Earth Sci. 167, 209–217. https://doi.org/10.1016/j.jseaes.2018.05.028.

Cumming, W., 2009. Geothermal resource conceptual models using surface exploration data. In: Proceedings of the 34th Workshop on Geothermal Reservoir Engineering. Stanford University, Stanford, CA.

Cumming, W., Mackie, R., 2010. Resistivity imaging of geothermal resources using 1D, 2D and 3D MT inversion and TDEM static shift correction illustrated by a Glass Mountain case history. In: Proceedings World Geothermal Congress 2010, pp. 25–29.

Egbert, G.D., Kelbert, A., 2012. Computational recipes for electromagnetic inverse problems. Geophys. J. Int. 189 (1), 251–267. https://doi.org/10.1111/j.1365-246X.2011.05347.x.

Galvão, M.S., Baroso, E.V., Leão, M.F., Mello, C.L., 2018. Fault zones control on permeability of poorly lithified sandstone. In: 52nd U.S. Rock Mechanics/Geomechanics Symposium. American Rock Mechanics Association. ARMA, Washington, D.C., pp. 18–1219

Grant, M.A., Bixley, P.F., 2011. Geothermal Reservoir Engineering, 2nd ed. Academic Press, pp. 1–28.

Guglielmetti, L., Comina, C., Abdelfettah, Y., Schill, E., Mandrone, G., 2013. Integration of 3D geological modeling and gravity surveys for geothermal prospection in an Alpine region. Tectonophysics 608, 1025–1036. https://doi.org/10.1016/j.tecto.2013.07.012.

Huang, C.S., 1991. The geological investigation of the Kanchiao fault, northern Taiwan. Bull, Cent. Geol., Surv. 7, 23–42 in Chinese with English abstract.

Huang, C.S., 1998. Geological Map of Taiwan, scale 1:50,000—Taipei. Central Geological Survey, 2nd ed. Ministry of Economic Affairs, Taipei, p. 62.

Huang, H.H., Wu, E.S., Lin, C.H., Ko, J.Y.T., Shih, M.H., Koulakov, I., 2021. Unveiling Tatun volcanic plumbing structure induced by post-collisional extension of Taiwan mountain belt. Sci. Rep. 11, 5286. https://doi.org/10.1038/s41598-021-84763-z.

Industrial Technology Research Institute (ITRI), 2015. High-efficiency Geothermal Energy Technology Research Project (1/3). Annual Execution Report of the Energy Technology Project of the Research Institution (104) (in Chinese).

Industrial Technology Research Institute (ITRI), 2021. Executive summary of geothermal exploration data in the Tatun Volcano Group Area (in Chinese). In: Report Commissioned by the Central Geological Survey, Ministry of Economic Affairs. Taiwan (in Chinese).

Johnston, J.M., Pellerin, L., Hohmann, G.W., 1992. Evaluation of electromagnetic methods for geothermal reservoir detection. Geotherm. Resour. Counc. Trans. 16, 241–245. https://doi.org/10.1190/1.1443931.

Jolie, E., Scott, S., Faulds, J., Chambefort, I., Axelsson, G., Negrín, L.C.G., Regenspurg, S., Ziegler, M., Ayling, M., Richter, A., Zemedkun, M.T., 2021. Geological controls on geothermal resources for power generation. Nat., Rev., Earth Env. 2, 324–339. https://doi.org/10.1038/s43017-021-00154-y.

Kelbert, A., Meqbel, N., Egbert, G.D., Tandon, K., 2014. ModEM: a modular system for inversion of electromagnetic geophysical data. Comput., Geosci. 66, 40–53. https://doi.org/10.1016/j.cageo.2014.01.010.

Keto, Y.K., Saïbi, H., 2021. Resistivity structure of Shalla-Abijata Geothermal Field, southwest Ethiopia using magnetotelluric data inversion. In: Proceedings World Geothermal Congress 2020. Reykjavik, Iceland, 26 April–2 May 2020.

Kim, K.H., Chiu, J.M., Pujol, J., Chen, K.C., Huang, B.S., Yeh, Y.H., Shen, P., 2005. Three-dimensional VP and VS structural models associated with the active subduction and collision tectonics in the Taiwan region. Geophys. J. Int. 162 (1), 204–220. https://doi.org/10.1111/j.1365-246X.2005.02657.x.

Komori, S., Utsugi, M., Kagiyama, T., Inoue, H., Chen, C.H., Chiang, H.T., Chao, B.F., Yoshimura, R., Kanda, W., 2014. Hydrothermal system in the Tatun Volcano Group, northern Taiwan, inferred from crustal resistivity structure by audio-magnetotellurics. Prog. Earth Planet. Sci. 1, 20. https://doi.org/10.1186/s40645-014-0020-7.

Komori, S., Utsugi, M., Kagiyama, T., Yoshikawa, S., Chen, C.H., Chao, B.F., 2017. Resistivity mapping in the Tatun Volcano Group, northern Taiwan, revealed by VLF-MT surveys. Terr. Atmos. Ocean. Sci. 28 (6), 833–842. https://doi.org/10.3319/TAO.2017.02.20.01.

Konstantinou, K.I., 2014. Potential for future eruptive activity in Taiwan and vulnerability to volcanic hazards. Nat. Hazard. 75, 2653–2671. https://doi.org/10.1007/s11069-014-1453-4.

Lan, C.Y., Liou, J.G., Seki, Y., 1980. Investigation of drillhole core samples from Tatun geothermal area, Taiwan. In: Proc. 3rd Int. Symp. Water–Rock Interaction. Edmonton, Canada, pp. 183–185.

Ledo, J., García-Merino, M., Larnier, H., Slezak, K., Piña-Varas, P., Marcuello, A., Queralt, P., Pérez, N.M., Schmincke, H.U., Sumita, M., 2021. 3D electrical resistivity of Gran Canaria island using magnetotelluric data. Geothermics 89, 101945. https://doi.org/10.1016/j.geothermics.2020.101945.

Lin, C.H., Konstantinou, K.I., Liang, W.T., Pu, H.C., Lin, Y.M., You, S.H., Huang, Y.P., 2005. Preliminary analysis of tectonic earthquakes and volcano-seismic signals recorded at the Tatun Volcanic Group, northern Taiwan. Geophys., Res., Lett. 32, L10313. https://doi.org/10.1029/2005GL022861.

Lin, T., Watts, A.B., Hesselbo, S.P., 2003. Cenozoic stratigraphy and subsidence history of the South China Sea margin in the Taiwan region. Basin Res 15, 453–478. https://doi.org/10.1046/j.1365-2117.2003.00215.x.

Lin, Y.P., Ko, J.Y.T., Huang, B.S., Lin, C.H., Shih, M.H., 2024. Unveiling attenuation structures in the northern Taiwan volcanic zone. Sci. Rep. 14, 4716. https://doi.org/10.1038/s41598-024-55397-8.

Lu, Y.C., Wang, C., Song, S.R., Wang, P.L., Song, T.J., Taguchi, S., Peng, T.R., Lin, L.H., Lee, J.C., Li, H.C., 2025. Characterization of neutral fluids in the volcanic geothermal system under the Tatun Volcano Group. Taiwan, J. Geochem., Explor. 278, 107814. https://doi.org/10.1016/j.gexplo.2025.107814.

Moeck, I.S., 2014. Catalog of geothermal play types based on geologic controls. Renew. Sustain. Energy Rev. 37, 867–882. https://doi.org/10.1016/j.rser.2014.05.032.

Muraoka, H., Uchida, T., Sasada, M., Yagi, M., Kohei Akaku, K., Sasaki, M., Yasukawa, K., Miyazaki, S., Doi, N., Saito, S., Sato, K., Tanaka, S., 1998. Deep geothermal resources survey program: igneous, metamorphic and hydrothermal processes in a well encountering 500 °C at 3729 m depth. Kakkonda Jpn., Geotherm. 27 (5–6), 507–534. https://doi.org/10.1016/S0375-6505(98)00031-5.

Ooz, Z., Ogaswara, M., 1934. 1:50,000 Scale Geological Map and instructions. Taiwan Governor-General's Office. Colonial Production Bureau.

Pearce, R.K., Sánchez de la Muele, A., Moorkamp, M., Hammond, J.O.S., Mitchell, T.M., Cembrano, J., Araya Vargas, J., Meredith, P.G., Iturrieta, P., Pérez-Estay, N., Marshall, N.R., Smith, J., Yañez, G., Ashley Griffith, W., Marquardt, C., Stanton-Yonge, A., Núñez, R., 2020. Reactivation of fault systems by compartmentalized hydrothermal fluids in the southern Andes revealed by magnetotelluric and seismic data. Tectonics 39 (1), e2019TC005997. https://doi.org/10.1029/2019TC005997.

Pu, H.C., Lin, C.H., Lai, Y.C., Shih, M.H., Li, Y.H., 2025. 4D seismic tomography unveiling velocity increase prior to seismic swarms at the Tatun Volcano Group of Taiwan. Sci. Rep. 15, 18220. https://doi.org/10.1038/s41598-025-02345-9.

Pu, H.C., Lai, Y.C., Shih, M.H., Chang, L.C., Lee, H.F., Lee, P.T., Hong, G.T., Li, Y.H., Chang, W.Y., Lo, C.H., 2020. Active volcanism revealed from a clustering seismicity conduit beneath the long-resting Tatun Volcano Group in northern. Taiwan, Sci., Rep. 10, 6153. https://doi.org/10.1038/s41598-020-63270-7.

Roquer, T., Arancibia, G., Rowland, J., Iturrieta, P., Morata, D., Cembrano, J., 2017. Fault-controlled development of shallow hydrothermal systems: structural and mineralogical insights from the southern Andes. Geothermics 66, 156–173. https://doi.org/10.1016/j.geothermics.2016.12.003.

Sawaki, T., Sasada, M., Sasaki, M., Goko, K., 1997. Fluid inclusion study of the Kirishima geothermal system. Jpn., Geotherm. 26 (3), 305–327. https://doi.org/10.1016/S0375-6505(96)00045-4.

Shyu, J.B.H., Sieh, K., Chen, Y.G., Liu, C.S., 2005. Neotectonic architecture of Taiwan and its implications for future large earthquakes. J. Geophys. Res.: Solid Earth 110 (B8), B08402. https://doi.org/10.1029/2004JB003251.

Sinotech Engineering Consultants, 2013. Atomic energy council, executive yuan, nuclear regulation department (2013). Offshore and onshore geological investigation results for the seismic safety re-evaluation enhancement of Nuclear power plants. In: Technical Report No. NRD-SER-102-02, September 2013. Taipei, Taiwan. (in Chinese).

Song, S., Tsao, S., Lo, C.H., 2000. Characteristics of the Tatun volcanic eruptions, North Taiwan: implications for a cauldron formation and volcanic eruption. J. Geol. Soc. China 43, 361–378.

Stimac, J., Goff, F., Janik, C., 2015. Intrusion-related geothermal systems. In: Sigurdsson, H. (Ed.), Encyclopedia of Volcanoes, 2nd ed. Elsevier, pp. 869–888.

Suppe, J., 1983. Geometry and kinematics of fault-bend folding. Am., J. Sci. 283, 684–721.

Suppe, J., 1985. Principles of Structural Geology. Prentice-Hall, Englewood Cliffs, NJ, p. 537.

Teng, L.S., 1996. Extensional collapse of the northern Taiwan mountain belt. Geology 24 (10), 949–952.

Teng, L.S., Chen, C.H., Wang, W.S., Liu, T.K., Juang, W.S., Chen, J.C., 1992. Plate kinematic model for late cenozoic arc magmatism in northern Taiwan. J. Geol. Soc. China 35, 1–18.

Teng, L.S., Lee, C.T., Peng, C.H., Chen, W.F., Chu, C.J., 2001. Origin and geological evolution of the Taipei Basin, northern Taiwan. West, Pac., Earth Sci. 1 (2), 115–142.

Yang, C.H., Shei, T.C., Lue, C.C., 1994. Gravity and magnetic studies in the Tatun Volcanic Region. Terr. Atmos. Ocean. Sci. 5, 499–514.

Yu, S.B., Chen, H.Y., Kuo, L.C., 1997. Velocity of GPS stations in the Taiwan area. Tectonophysics 274, 41–59.